

Hybrid σ - p Coordinate Choices for a Global Model

STEPHEN ECKERMANN

Space Science Division, Naval Research Laboratory, Washington, D.C.

(Manuscript received 18 January 2008, in final form 23 June 2008)

ABSTRACT

A methodology for choosing a hybrid σ - p (sigma-pressure) vertical coordinate of the Simmons–Strüfing form for a global model is presented. The method focuses on properties of the vertical derivative of the terrain-following coefficient, which affect the smoothness and shape of layer thickness profiles and determines the coordinate’s monotonicity over variable terrain. The method is applied to characterize and interrelate existing hybrid coordinate choices in NWP and climate models, then to design new coordinates with specific properties. Offline tests indicate that the new coordinates reduce stratospheric errors in models due to vertical truncation effects in the computation of the pressure gradient force over steep terrain. When implemented in a global model, the new coordinates significantly reduce vorticity and divergence errors at all altitudes in idealized simulations. In forecasting experiments with a global model, the new coordinates slightly reduce the stability of the semi-implicit time scheme. Resetting the reference pressure in the scheme to ~ 800 hPa solves the problem for every coordinate except the Sangster–Arakawa–Lamb hybrid, which remains intrinsically less stable than the others. Impacts of different coordinates on forecast skill are neutral or weakly positive, with the new hybrid coordinates yielding slight improvements relative to earlier hybrid choices. This essentially neutral impact indirectly endorses the wide variety of hybrid coordinate choices currently used in NWP and climate models, with the proviso that these tests do not address the impact over longer time scales or on data assimilation.

1. Introduction

Many global models solve the hydrostatic primitive equations on the sphere using a generalized vertical coordinate, based on equation sets first derived in continuous form by Kasahara (1974) and in discretized form by Simmons and Burridge (1981). Given pressure p as the physical altitude variable, this coordinate can take the functional form:

$$\eta = h(p, p_S), \quad (1)$$

where p_S is the surface pressure and $h(p, p_S)$ is a monotonic function of p , such that there is a one-to-one mapping between p and η for a given p_S . The functional dependence on p_S permits terrain-following coordinates. The standard convention is to define η to be normalized and dimensionless, satisfying the lower and upper boundary conditions:

$$h(p_S, p_S) = 1, \quad (2)$$

$$h(p_{\text{top}}, p_S) = 0, \quad (3)$$

respectively, where p_{top} is the pressure at the top model half-layer. The chain rule applied to (1) allows η terms in the equations to be reexpressed in terms of p , p_S , and p_{top} , which has the practical advantage that η need not be defined explicitly.

The most straightforward choice for η is the terrain-following σ coordinate, obtained by setting

$$\eta = h(p, p_S) = \frac{p - p_{\text{top}}}{p_S - p_{\text{top}}} = \sigma. \quad (4)$$

This is a minor generalization of the original Phillips (1957) σ coordinate p/p_S for models with a nonvanishing p_{top} (Mintz 1965).

However, as models extend into the middle atmosphere, there are numerical and practical advantages in choosing a function $h(p, p_S)$ that smoothly transitions η from terrain-following levels near the ground to isobaric surfaces in the upper troposphere or lower stratosphere (Fels et al. 1980; Simmons and Burridge 1981; Simmons and Strüfing 1983; Simmons et al. 1989). Sim-

Corresponding author address: Stephen Eckermann, Space Science Division, Code 7646, Naval Research Laboratory, 4555 Overlook Ave. SW, Washington, DC 20375.
E-mail: stephen.eckermann@nrl.navy.mil

Report Documentation Page

Form Approved
OMB No. 0704-0188

Public reporting burden for the collection of information is estimated to average 1 hour per response, including the time for reviewing instructions, searching existing data sources, gathering and maintaining the data needed, and completing and reviewing the collection of information. Send comments regarding this burden estimate or any other aspect of this collection of information, including suggestions for reducing this burden, to Washington Headquarters Services, Directorate for Information Operations and Reports, 1215 Jefferson Davis Highway, Suite 1204, Arlington VA 22202-4302. Respondents should be aware that notwithstanding any other provision of law, no person shall be subject to a penalty for failing to comply with a collection of information if it does not display a currently valid OMB control number.

1. REPORT DATE 23 JUN 2008		2. REPORT TYPE		3. DATES COVERED 00-00-2008 to 00-00-2008	
4. TITLE AND SUBTITLE Hybrid o-p (sigma-pressure) Coordinate Choices for a Global Model				5a. CONTRACT NUMBER	
				5b. GRANT NUMBER	
				5c. PROGRAM ELEMENT NUMBER	
6. AUTHOR(S)				5d. PROJECT NUMBER	
				5e. TASK NUMBER	
				5f. WORK UNIT NUMBER	
7. PERFORMING ORGANIZATION NAME(S) AND ADDRESS(ES) Naval Research Laboratory,Space Science Division,Washington,DC,20375				8. PERFORMING ORGANIZATION REPORT NUMBER	
9. SPONSORING/MONITORING AGENCY NAME(S) AND ADDRESS(ES)				10. SPONSOR/MONITOR'S ACRONYM(S)	
				11. SPONSOR/MONITOR'S REPORT NUMBER(S)	
12. DISTRIBUTION/AVAILABILITY STATEMENT Approved for public release; distribution unlimited					
13. SUPPLEMENTARY NOTES					
14. ABSTRACT see report					
15. SUBJECT TERMS					
16. SECURITY CLASSIFICATION OF:			17. LIMITATION OF ABSTRACT	18. NUMBER OF PAGES	19a. NAME OF RESPONSIBLE PERSON
a. REPORT unclassified	b. ABSTRACT unclassified	c. THIS PAGE unclassified			

mons and Strüfing (1981) and Simmons and Burridge (1981) tested different functional forms for $h(p, p_S)$ that yielded so-called hybrid σ - p coordinates. The final function considered by Simmons and Strüfing (1981) took the implicit form

$$p(\tilde{\eta}, p_S) = \hat{A}(\tilde{\eta})p_0 + \hat{B}(\tilde{\eta})p_S, \quad (5)$$

where p_0 is some nominal sea level pressure, typically ~ 1000 hPa, and $\tilde{\eta}$ is the corresponding vertical profile of η values for $p_S = p_0$. Later, Simmons and Strüfing (1983) replaced $\hat{A}(\tilde{\eta})p_0$ with the simpler form $A(\tilde{\eta})$. Generalizing to a nonzero p_{top} yields

$$p(\tilde{\eta}, p_S) = A(\tilde{\eta}) + B(\tilde{\eta})(p_S - p_{\text{top}}), \quad (6)$$

to satisfy the upper-level boundary condition in (3). A corresponding explicit expression for η that satisfies the boundary conditions (2) and (3) is

$$\eta = \frac{p - p_{\text{top}}}{p_S - p_{\text{top}}} = \frac{A(\tilde{\eta}) - p_{\text{top}}}{p_S - p_{\text{top}}} + B(\tilde{\eta}), \quad (7)$$

such that $p_{\text{top}} \leq A(\tilde{\eta}) \leq p$, $0 \leq B(\tilde{\eta}) \leq 1$, and $dB/d\tilde{\eta} \geq 0$.

This coordinate is defined by vertical profiles of the two coefficients, A and B , which control, respectively, its isobaric and terrain-following properties. For $B \neq 0$, the coordinate has terrain-following properties, from (6), of the following form:

$$B(\tilde{\eta}) = \frac{p - A(\tilde{\eta})}{p_S - p_{\text{top}}}. \quad (8)$$

By analogy to (4), (8) implies a σ -like coordinate on the reference level $\tilde{\eta}$ in which the effective model top is not p_{top} , but $A(\tilde{\eta})$. Since σ surfaces of the form in (4) flatten out as $p \rightarrow p_{\text{top}}$ (see Fig. 1 of Hogan and Rosmond 1991) and $A(\tilde{\eta}) \geq p_{\text{top}}$, (8) yields a surface whose response to terrain has been reduced, or flattened, relative to pure σ (4) when $A(\tilde{\eta}) > p_{\text{top}}$.

While more elaborate functional forms for $h(p, p_S)$ can be chosen (e.g., Simmons and Burridge 1981; Arakawa and Konor 1996), the Simmons and Strüfing (1983) form in (6) has proven sufficiently flexible that it is now built into the dynamical cores of many numerical weather prediction (NWP) and climate models. Furthermore (6) can be used, with minor modifications, in nonhydrostatic dynamical cores (Laprise 1992; Wood and Staniforth 2003), and can be extended to accommodate more sophisticated hybrid formulations, such

as isentropic levels θ through a hybrid σ - θ - p coordinate of a similar functional form in which h is now also a function of temperature (e.g., Zhu et al. 1992; Webster et al. 1999).

Yet, despite its widespread use in NWP and climate models, there is no specific guidance in the literature on how best to set the governing coefficients $A(\tilde{\eta})$ and $B(\tilde{\eta})$ to provide an appropriate hybrid coordinate for a given modeling application. Simmons and Burridge (1981), who presented subsets of the results in Simmons and Strüfing (1981), did not consider hybrid coordinates of the form in (6) at all (apart from a brief footnote added in proof). While presenting a series of important model tests relevant to the choice of a hybrid coordinate, Simmons and Burridge (1981) explicitly made no specific recommendations about which hybrid coordinate to use, noting choices were dependent on specific modeling application and spatial resolution. The global modeling study of Simmons and Strüfing (1983) compared several different hybrid-coordinate and σ -coordinate forecasts, finding small forecasting improvements with hybrid coordinates and limited differences in model performance among the various hybrid coordinates they tested. Again, no specific guidance on an optimal choice for $A(\tilde{\eta})$ and $B(\tilde{\eta})$ was provided, apart from one hybrid coordinate which rendered their model more unstable numerically and was discarded. Due perhaps to the small effects on forecast skill noted by Simmons and Strüfing (1983), there have been no subsequent tests of hybrid σ - p coordinates reported in the literature.

The main purpose of this paper is to set forth a straightforward methodology for designing and testing hybrid σ - p vertical coordinates of the Simmons and Strüfing (1983) form for a global model. In section 2, we show that the coordinate's relevant properties, such as smoothness and shape preservation of layer thickness profiles and monotonicity over high terrain, are encapsulated in the vertical gradient of the terrain-following coefficient, $dB/d\tilde{\eta}$. We apply these $dB/d\tilde{\eta}$ diagnostics in section 3 to introduce and characterize a series of hybrid vertical coordinates used previously in models, but now all expressed in the Simmons and Strüfing (1983) form in (6). In section 4 we use the same diagnostics to design some new hybrid coordinates with specific properties. Section 5 studies the errors in the pressure gradient force produced by these coordinates over steep terrain due to truncation effects of the global model's vertically discretized finite-difference formulation. Section 6 implements and tests hybrid coordinates in an advanced-level physics high-altitude (ALPHA) prototype of the Navy Operational

Global Atmospheric Prediction System (NOGAPS), to investigate their effects on model errors, stability, and forecast skill. Our findings, along with coordinate choices used in other climate and NWP models, are summarized in section 7.

2. Formulation and diagnostics

a. Discretization

In σ -coordinate models it is common to tag model levels by their invariant σ values. This fails for hybrid coordinates: from (7), any isobaric component to the

coefficient [$A(\tilde{\eta}) > p_{\text{top}}$] causes η values to vary with surface pressure. Thus, we tagged model levels initially in section 1 using the profile $\tilde{\eta}$ evaluated at a constant nominal sea level pressure p_0 , such that $A(\tilde{\eta})$ and $B(\tilde{\eta})$ are the invariant values of the isobaric and terrain-following coefficients, respectively, on a given model level $\tilde{\eta}$.

In discretized form, full model levels (layers) are tagged from top to bottom with indices $k = 1, \dots, L$, where L is the total number of layers. Pressures on the $L + 1$ half (interface) levels are specified using the hybrid σ - p function (6):

$$\begin{aligned} p(\tilde{\eta}_{k+1/2}, p_S) &= A(\tilde{\eta}_{k+1/2}) + B(\tilde{\eta}_{k+1/2})(p_S - p_{\text{top}}), \text{ now equivalently} \\ p_{k+1/2} &= A_{k+1/2} + B_{k+1/2}(p_S - p_{\text{top}}). \end{aligned} \quad (9)$$

To reproduce p_{top} and p_S at the top and bottom half levels, respectively, the boundary conditions for (9), analogous to (2) and (3), are

$$\begin{aligned} A(0) &= A_{1/2} = p_{\text{top}} & B(0) &= B_{1/2} = 0, \\ A(1) &= A_{L+1/2} = p_{\text{top}} & B(1) &= B_{L+1/2} = 1. \end{aligned} \quad (10)$$

Layer thicknesses are

$$\Delta p_k = p_{k+1/2} - p_{k-1/2} = \Delta A_k + \Delta B_k(p_S - p_{\text{top}}), \quad (11)$$

where

$$\begin{aligned} \Delta A_k &= A_{k+1/2} - A_{k-1/2}, \\ \Delta B_k &= B_{k+1/2} - B_{k-1/2}. \end{aligned} \quad (12)$$

From (7), (12) also defines the model's η layer thicknesses:

$$\Delta \eta_k = \frac{\Delta A_k}{p_S - p_{\text{top}}} + \Delta B_k. \quad (13)$$

The $\tilde{\eta}$ levels, evaluated at a nominal sea level surface pressure $p_0 \sim 1000$ hPa, yield corresponding half-level pressures $\tilde{p}_{k+1/2}$, such that $\tilde{p}_{L+1/2} = p_0$. Consider now a surface pressure p_S that differs from this nominal sea level value $\tilde{p}_{L+1/2}$. Using (9) we can express the new pressure levels $p_{k+1/2}$ and layer pressure thicknesses Δp_k as departures from the nominal profiles $\tilde{p}_{k+1/2}$ and $\Delta \tilde{p}_k$:

$$p_{k+1/2} = \tilde{p}_{k+1/2} + B_{k+1/2}(p_S - \tilde{p}_{L+1/2}), \quad (14)$$

$$\Delta p_k = \Delta \tilde{p}_k + \Delta B_k(p_S - \tilde{p}_{L+1/2}). \quad (15)$$

In the limit of an infinitesimal surface pressure change, (15) can be reexpressed as

$$\frac{\partial \Delta p_k}{\partial p_S} = \Delta B_k. \quad (16)$$

b. Shape preservation of layer thickness profiles

Vertical profiles of pressure thicknesses $\Delta \tilde{p}_k$ are carefully chosen in global models. Figure 1 plots representative profiles of $\Delta \tilde{p}_k$ and the corresponding pressure-height thicknesses $\Delta \tilde{Z}_k$, the latter computed from pressure altitudes,

$$Z_{k+1/2} = H \ln \left(\frac{p_0}{p_{k+1/2}} \right), \quad (17)$$

using $p_0 = 1000$ hPa and $H = 7$ km. The different curves compare the operational NOGAPS L30 and research NOGAPS-ALPHA L60 and L84 thicknesses with some other operational configurations used in the European Centre for Medium-Range Weather Forecasts (ECMWF) Integrated Forecast System (IFS) and National Centers for Environmental Prediction (NCEP) Global Forecast System (GFS). In addition to concentrating layers in preferred regions such as the boundary layer, these profiles vary thicknesses smoothly across adjacent layers in to order to minimize introduction of errors through the model's vertical finite-difference calculations.

Equation (16) determines how these thickness profiles respond over terrain. We assume choices for $B(\tilde{\eta})$ that vary B values sufficiently gradually in comparison

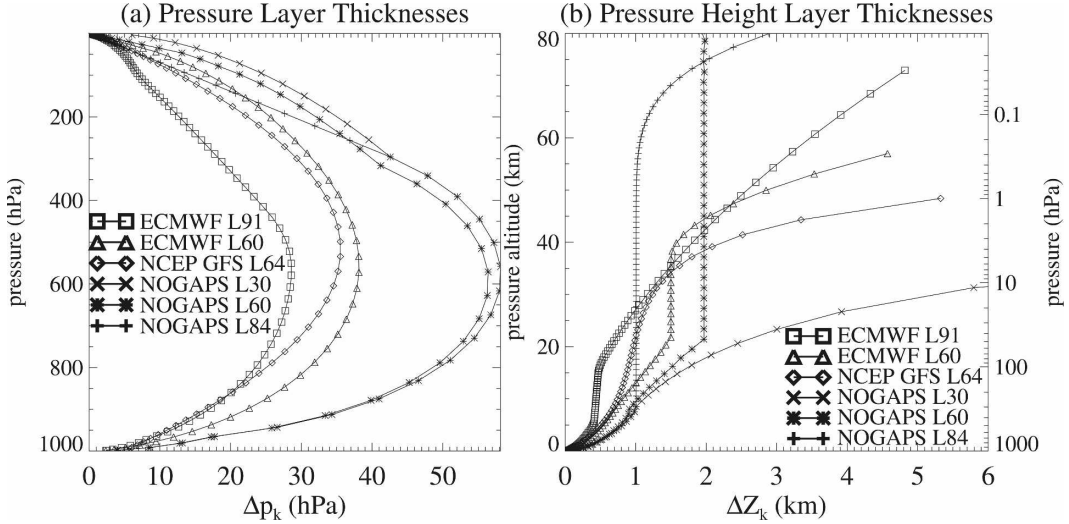


FIG. 1. Plot of layer thicknesses (a) $\Delta \tilde{p}_k$ and (b) $\Delta \tilde{Z}_k$ vs \tilde{p}_k and \tilde{Z}_k , respectively. Results are shown for two recent ECMWF IFS configurations (L91, L60), the operational NOGAPS L30 levels, two sets of NOGAPS-ALPHA levels (L60, L84), and a recent set of operational NCEP GFS L64 levels.

to model layer thicknesses that the linear approximation

$$\Delta B_k \approx \left(\frac{dB}{d\tilde{\eta}} \right)_k \Delta \tilde{\eta}_k \quad (18)$$

is accurate, whereupon (15) can be reexpressed as

$$\Delta p_k \approx \Delta \tilde{p}_k + \left(\frac{dB}{d\tilde{\eta}} \right)_k \Delta \tilde{\eta}_k (p_S - \tilde{p}_{L+1/2}). \quad (19)$$

Since $\Delta \tilde{\eta}_k = \Delta \tilde{p}_k / (\tilde{p}_{L+1/2} - p_{\text{top}})$, we can reexpress (19) as

$$\Delta p_k = \Delta \tilde{p}_k \left[1 + \left(\frac{dB}{d\tilde{\eta}} \right)_k \left(\frac{\Delta p_S}{\tilde{p}_{L+1/2} - p_{\text{top}}} \right) \right], \quad (20)$$

where $\Delta p_S = p_S - \tilde{p}_{L+1/2}$ is the change in surface pressure from the nominal sea level value $\tilde{p}_{L+1/2}$. The multiplicative term in square parentheses in (20):

$$s(\tilde{\eta}, p_S) = 1 + \left(\frac{dB}{d\tilde{\eta}} \right)_k \left(\frac{\Delta p_S}{\tilde{p}_{L+1/2} - p_{\text{top}}} \right), \quad (21)$$

is a ‘‘shape factor’’ that modifies the values and shape of the reference thickness profile $\Delta \tilde{p}_k$ over terrain, such that the new profile is

$$\Delta p_k = \Delta \tilde{p}_k s(\tilde{\eta}_k, p_S). \quad (22)$$

From (22), we get perfect shape preservation of pressure thickness profiles when $\partial s / \partial \tilde{\eta} = 0$, or equivalently from (21) when $dB/d\tilde{\eta}$ is a constant.

The definition in (1) requires η to be a monotonic function of p for all possible surface pressures p_S in the model. We can check this by testing for surface

pressures that yield vanishing thicknesses Δp_k , which from (22) occur at any level $\tilde{\eta}$ where $s(\tilde{\eta}_k, p_S) = 0$. From (21), this latter criterion can be expressed equivalently as

$$\frac{dB/d\tilde{\eta} - 1}{dB/d\tilde{\eta}} = \frac{(p_S)_{\min} - p_{\text{top}}}{\tilde{p}_{L+1/2} - p_{\text{top}}}. \quad (23)$$

For any $B(\tilde{\eta})$, $(p_S)_{\min}$ in (23) is the minimum surface pressure that this coordinate can tolerate before becoming nonmonotonic.

c. Setting $A(\tilde{\eta})$ and $B(\tilde{\eta})$

The primary importance of $dB/d\tilde{\eta}$ in defining the salient characteristics of hybrid coordinates of the Simmons and Strüfing (1983) form (6) implies that its required form should drive algorithms for setting the coefficients $A_{k+1/2}$ and $B_{k+1/2}$ in a model. A flexible and fairly general algorithm for assigning $A_{k+1/2}$ and $B_{k+1/2}$ values based on this philosophy is described in the appendix.

The algorithm allows the top k_p model layers to be isobaric and lowest k_σ model layers to be σ -like. The intervening model layers $k = k_p + 1, \dots, L - k_\sigma$ take a hybrid form defined by terrain-following coefficients of the analytical form:

$$B(\tilde{\eta}) = \left(\frac{\tilde{\eta} - \tilde{\eta}_{k_p+1/2}}{1 - \tilde{\eta}_{k_p+1/2}} \right)^{r(\tilde{\eta})} = b(\tilde{\eta})^{r(\tilde{\eta})}. \quad (24)$$

The $A(\tilde{\eta})$ values follow from (7) using the reference values $\eta = \tilde{\eta}$ and $p_S = \tilde{p}_{L+1/2}$.

The terrain-following coefficient gradient is given by the analytical expression:

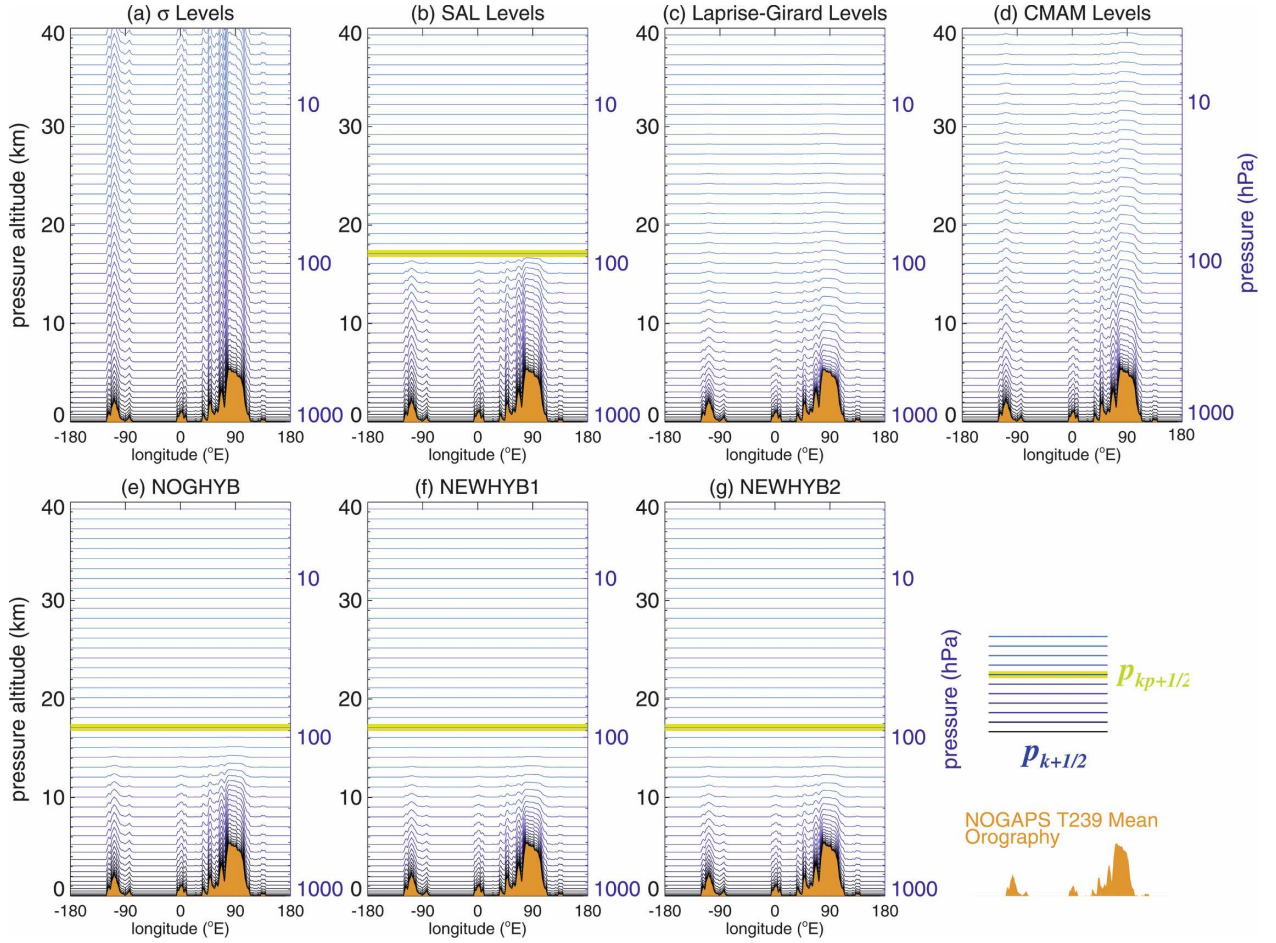


FIG. 2. T239L84 half-levels $p_{k+1/2}$ at $\sim 34.7^\circ\text{N}$ from $Z_{k+1/2} = 0\text{--}40$ km for all vertical coordinates tested in NOGAPS-ALPHA (see Table 1): (a) σ , (b) SAL, (c) LG, (d) CMAM, (e) original NOGAPS-ALPHA hybrid (NOGHYB), and (f), (g) two new NOGAPS-ALPHA hybrids (NEWHYB1, NEWHYB2). The $p_{k+1/2}$ contours are color coded, with light (dark) blue lines indicating $B_{k+1/2}$ near zero (unity). Green curves show the lowest-altitude isobaric level $p_{k_p+1/2} = 86.7$ hPa ($k_p = 58$) for the coordinates with $k_p > 0$. T239 topographic elevations are shaded light brown.

$$\frac{dB}{d\tilde{\eta}} = \begin{cases} 0 & k = 1, \dots, k_p, \\ \frac{r(\tilde{\eta})b(\tilde{\eta})^{r(\tilde{\eta})-1}}{1 - \tilde{\eta}_{k_p+1/2}} + b(\tilde{\eta})^{r(\tilde{\eta})} \left(\frac{dr}{d\tilde{\eta}} \right) \ln b(\tilde{\eta}) & k = k_p + 1, \dots, L - k_\sigma, \\ (1 - \tilde{\eta}_{k_p+1/2})^{-1} & k = L + 1 - k_\sigma, \dots, L. \end{cases} \quad (25)$$

Thus, the form of this hybrid coordinate, defined by (25), is dictated solely by the choices for k_p , k_σ , and the power-law index profile $r(\tilde{\eta})$, which are varied until a coordinate with the requisite $dB/d\tilde{\eta}$ properties is obtained.

3. Examples

We use the algorithm described in section 2c to introduce some basic hybrid coordinates, which we then

characterize using the $dB/d\tilde{\eta}$ -based diagnostic tools of section 2b.

a. σ coordinate

The σ coordinate [(4)] is recovered by setting $k_p = 0$ and $k_\sigma = L$, or equivalently by setting $k_p = k_\sigma = 0$ and $r(\tilde{\eta}_{k+1/2}) = r_{k+1/2} = 1$. Resulting half-levels around a 34.7°N latitude circle are plotted in Fig. 2a for a T239L84 NOGAPS-ALPHA model resolution (see Fig. 1).

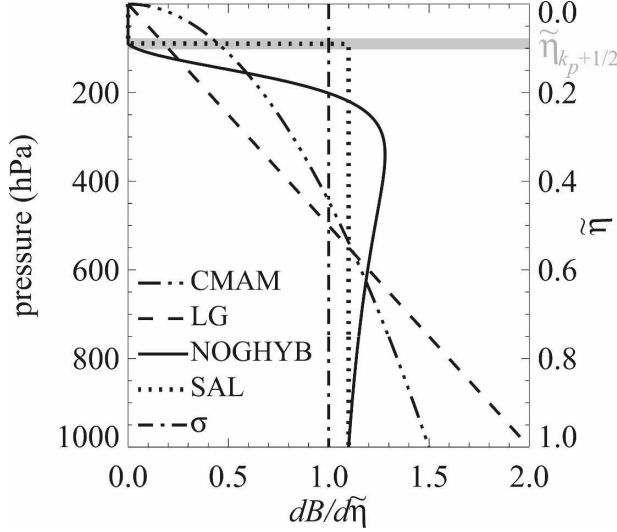


FIG. 3. Profiles of $dB/d\tilde{\eta}$ for the vertical coordinates discussed in section 3 (see Table 1).

Our diagnostic tools of section 2b illustrate some of the advantages of this coordinate. Since $A(\tilde{\eta}) = p_{\text{top}}$ and $B(\tilde{\eta}) = \tilde{\eta}$, then $dB/d\tilde{\eta} = 1$ and $\partial s/\partial \tilde{\eta} = 0$ for all $\tilde{\eta}$. Thus, the σ coordinate perfectly preserves the shapes of the model thickness profiles $\Delta\tilde{p}_k$ in Fig. 1a. Furthermore, the monotonicity criterion in (23) yields $(p_S)_{\text{min}} = p_{\text{top}}$. Thus, the coordinate is always monotonic so long as mountain peaks do not breach the top of the model.

The shape-preserving $dB/d\tilde{\eta} = 1$ profile of the σ coordinate is plotted in Fig. 3.

b. Sangster–Arakawa–Lamb coordinate

This hybrid coordinate is used in a number of climate models (e.g., Cariolle and Déqué 1986; Eluszkiewicz et al. 2000; Collins et al. 2004), and is perhaps the most straightforward to implement and visualize. In the terrain-following region $k > k_p$, it has the analytical form $(p - \tilde{p}_{k_p+1/2})/(p_S - \tilde{p}_{k_p+1/2})$ (Arakawa and Lamb 1977). Thus, it consists of a σ coordinate in (4) formulated between the surface and $p_{k_p+1/2}$, with isobaric model layers stacked on top between $p_{k_p+1/2}$ and p_{top} . While Haltiner and Williams (1980) and Simmons and Burridge (1981) attribute this coordinate to Arakawa and Lamb (1977), who derived it for use in the University of California, Los Angeles (UCLA) general circulation model (Schlesinger and Mintz 1979), it was derived earlier by Sangster (1960), whose ideas were used to build this coordinate into the Geophysical Fluid Dynamics Laboratory (GFDL) SKYHI model (Fels et al. 1980). Thus, here we refer to it as the Sangster–Arakawa–Lamb (SAL) coordinate. Simmons and Strüfing (1981) referred to it as the “traditional” hybrid coordinate.

For models using the Simmons and Strüfing (1983)

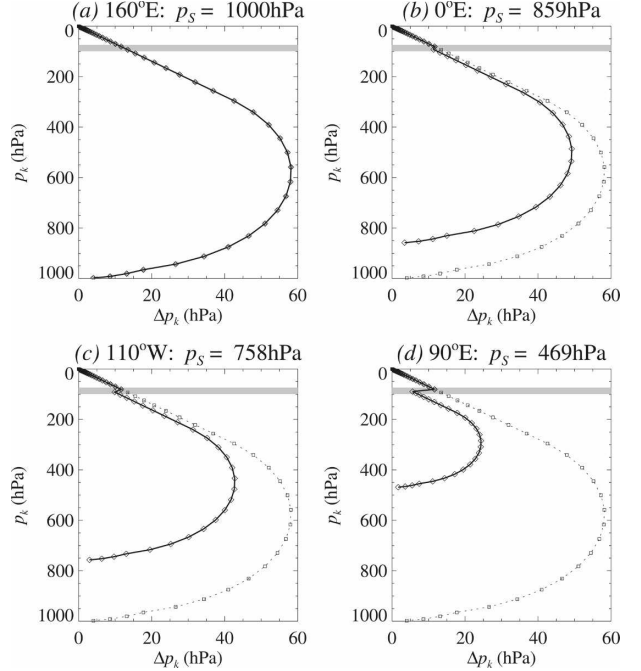


FIG. 4. Solid curve shows response of L84 layer pressure thicknesses Δp_k vs p_k for the SAL coordinate at four selected longitudes in Fig. 2b with progressively higher terrain: (a) 160°E, (b) 0°E, (c) 110°W, and (d) 90°E. Surface pressures p_S , given in plot title, are calculated as $p_0 \exp(-h'/H)$ where h' is topographic elevation, $H = 7$ km, and $p_0 = 1000$ hPa. The dotted curve in each panel shows thicknesses $\Delta\tilde{p}_k$ for $p_S = p_0$. Gray line shows the lowest pure pressure interface level at $p_{k_p+1/2} \approx 86.7$ hPa ($k_p = 58$).

form in (6), it is obtained by setting $r_{k+1/2} = 1$ in (24). The terrain-following layers $k > k_p$ then assume SAL forms for any k_σ in the range $0 \leq k_\sigma \leq L - k_p$ (see the appendix) of $B_{k+1/2} = b_{k+1/2}$ and $A_{k+1/2} = \tilde{p}_{k_p+1/2} + b_{k+1/2}(p_{\text{top}} - \tilde{p}_{k_p+1/2})$. Figure 2b plots these SAL half levels using the L84 reference levels in Fig. 1a with $k_p = 58$, which yields a lowest isobaric half-level of $\tilde{p}_{k_p+1/2} = 86.7$ hPa (shown in green). From (25), the terrain-following coefficient derivative

$$\frac{dB}{d\tilde{\eta}} = \begin{cases} 0 & k = 1, \dots, k_p, \\ (1 - \tilde{\eta}_{k_p+1/2})^{-1} & k = k_p + 1, \dots, L, \end{cases} \quad (26)$$

which is plotted as the dotted curve in Fig. 3. Inserting (26) into the monotonicity criterion (23) yields $(p_S)_{\text{min}} = \tilde{p}_{k_p+1/2}$.

The constant terrain-following coefficient gradients in (26) imply constant shape factors $s(\tilde{\eta}_k, p_S)$ and hence shape preservation of pressure thicknesses Δp_k , with one important exception: a sharp discontinuity in $dB/d\tilde{\eta}$ at the $k_p + 1/2$ interface (see Fig. 3). Profiles of Δp_k in Fig. 4, taken at selected longitudes in Fig. 2b with progressively higher terrain, reveal the resulting effect on

layer thicknesses in the L84 model. While the σ -like nature of the coordinate at lower altitudes yields perfect shape preservation, this $dB/d\tilde{\eta}$ change across the $k_p + 1/2$ interface produces a large Δp_k discontinuity over high terrain (see Fig. 4d). The discontinuity is even more apparent in the corresponding pressure–height thicknesses ΔZ_k in Fig. 5. Such discontinuities can yield large errors in the model’s vertical finite-difference calculations, potentially triggering erroneous gravitational instabilities over high terrain and greater computational instability of the semi-implicit time scheme (Simmons and Burridge 1981). We return to the issue of model stability in section 6b.

c. Laprise–Girard coordinate

This coordinate, developed by Laprise and Girard (1990) for the Canadian Climate Center (CCC) model (McFarlane et al. 1992), is recovered by setting $r_{k+1/2} = 2$. While Laprise and Girard (1990) did not impose any isobaric layers ($k_p = 0$), it is straightforward to generalize to nonzero k_p . To avoid a thickness discontinuity across the $L - k_\sigma + 1/2$ interface analogous to that for the SAL coordinate at $k_p + 1/2$, we must set $k_\sigma = 0$ here.

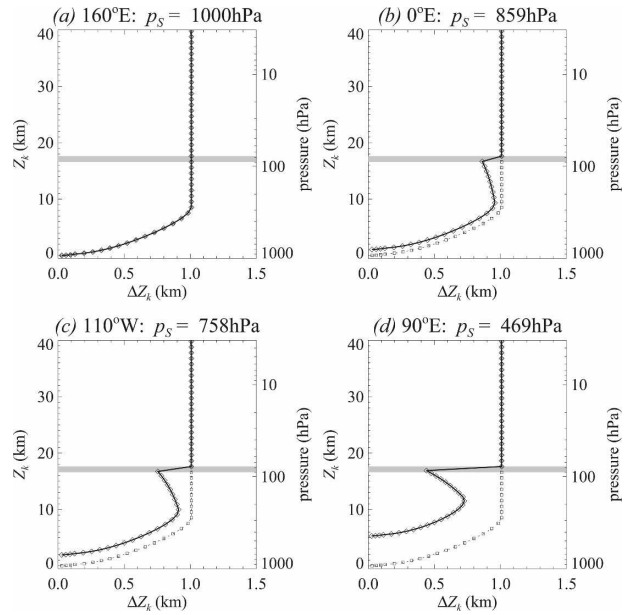


FIG. 5. As in Fig. 4, but profiling the SAL-coordinate response of L84 pressure–height layer thicknesses ΔZ_k vs Z_k (solid) relative to the L84 profile ΔZ_k at $p_s = p_0$ (dotted; see Fig. 1b).

From (25), these choices yield

$$\frac{dB}{d\tilde{\eta}} = \begin{cases} 0 & k = 1, \dots, k_p, \\ 2(\tilde{\eta} - \tilde{\eta}_{k_p+1/2})(1 - \tilde{\eta}_{k_p+1/2})^{-2} & k = k_p + 1, \dots, L, \end{cases} \quad (27)$$

which is plotted as the dashed curve in Fig. 3 using $k_p = 0$. Substituting the latter expression in (27) into the monotonicity criterion (23) yields

$$[(p_s)_{\min}]_{k+1/2} = p_{\text{top}} + (\tilde{p}_{L+1/2} - p_{\text{top}}) \left(1 + \frac{\tilde{\eta}_{k_p+1/2} - 0.5}{\tilde{\eta}_{k+1/2} - \tilde{\eta}_{k_p+1/2}} \right), \quad (28)$$

which maximizes at the surface ($\tilde{\eta}_{L+1/2} = 1$) to yield

$$[(p_s)_{\min}]_{L+1/2} = 0.5\tilde{p}_{L+1/2}, \quad (29)$$

(Laprise and Girard 1990). For $\tilde{p}_{L+1/2} = p_0 \sim 1000$ hPa, this yields vanishing layer thicknesses at the surface when surface pressures over high terrain drop below ~ 500 hPa.

Figure 2c plots Laprise–Girard (LG) coordinate surfaces for the NOGAPS-ALPHA L84 thicknesses in Fig. 1a. The coordinate surfaces transition naturally to quasi-isobaric levels in the stratosphere, explaining why Laprise and Girard (1990) implemented it without an explicit transition to pure pressure levels ($k_p = 0$). However, over the Himalayas, where our idealized surface pressure calculation yields $p_s = 469$ hPa, the thick-

nesses in Fig. 2c become negative at the surface, yielding subterranean model levels, consistent with (29). This coordinate is evidently stable in climate models due to their low horizontal resolutions, which reduce peak terrain heights and increase minimum terrain pressures. Clearly this coordinate is more prone to violating monotonicity in models with higher horizontal resolution.

This probably explains the recent transition of the higher-resolution Canadian Middle Atmosphere Model (CMAM), a CCC climate model derivative, from $r_{k+1/2} = 2$ to $r_{k+1/2} = 1.5$ (Polavarapu et al. 2005), which reduces $(p_s)_{\min}/\tilde{p}_{L+1/2}$ from 1/2 to 1/3. The resulting $dB/d\tilde{\eta}$ profile is plotted as the dot–dashed curve in Fig. 3. The corresponding CMAM coordinate surfaces are plotted in Fig. 2d, showing that the improved mono-

tonicity of this modified coordinate comes at the expense of a more gradual transition with altitude from terrain-following to isobaric levels.

d. Initial NOGAPS-ALPHA (NOGHYB) coordinate

NOGAPS-ALPHA is a high-altitude prototype of the NOGAPS NWP system (Allen et al. 2006). One aspect of that extension was to replace the σ levels used operationally with hybrid levels that transitioned to pressure surfaces in the new middle-atmosphere layers (Eckermann et al. 2004). To have as little impact as possible on NOGAPS tropospheric NWP performance, the goal initially was to use model levels from ~ 1000 to 400 hPa that were as close as possible to the operational model's pure σ levels, before transitioning to newer hybrid σ - p layers at higher altitudes. These choices are reflected in the thickness profiles in Fig. 1: the NOGAPS-ALPHA L60 and L84 thickness profiles largely track the operational L30 thicknesses from 1000 to 400 hPa, departing in shape thereafter.

The hybrid coordinate that best retains σ -like tropospheric layers is the SAL coordinate, but its major drawback, highlighted in section 3b, is the sharp discontinuity in layer thicknesses over high terrain at $k_p + 1/2$ (Fig. 4) and the potential impact on model errors and stability (Simmons and Strüfing 1983). Thus, the hybrid coordinate implemented in NOGAPS-ALPHA used the algorithm outlined in section 2c with a power index of the following form:

$$r(\tilde{\eta}) = r_p + \frac{(r_\sigma - r_p)}{\arctan S} \arctan[Sb(\tilde{\eta})], \quad (30)$$

where r_σ is the limiting index at $L - k_\sigma + 1/2$, r_p is the limiting index at $k_p + 1/2$, and S is a dimensionless constant that controls the smooth transition to each limiting value, such that

$$\frac{dr(\tilde{\eta})}{d\tilde{\eta}} = \frac{(r_\sigma - r_p)}{\arctan S} \frac{S}{\{1 + [Sb(\tilde{\eta})]^2\}} \frac{1}{(1 - \tilde{\eta}_{k_p+1/2})}, \quad (31)$$

for use in (25). For $k_\sigma \neq 0$, we require $r_\sigma = 1$ to avoid thickness discontinuities across the $L - k_\sigma + 1/2$ interface.

We eventually settled upon $r_p = 2$, $r_\sigma = 1$, and $S = 10$. These NOGHYB coordinate settings are listed in Table 1 and its $dB/d\tilde{\eta}$ profile is plotted as the solid curve in Fig. 3. For $\tilde{p}_{k_p+1/2} \lesssim 100$ hPa, these choices yield a SAL-like coordinate ($r \approx 1$) at 1000 hPa $\lesssim \tilde{p}_{k+1/2} \lesssim 400$ hPa, followed by a fairly sharp transition to the LG-coordinate limit of $r \rightarrow 2$ as $\tilde{\eta} \rightarrow \tilde{\eta}_{k_p+1/2}$,

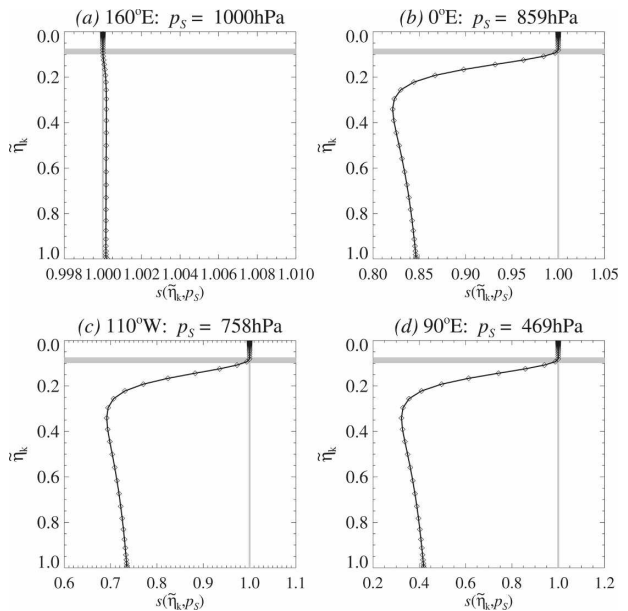


FIG. 6. NOGHYB coordinate shape factors $s(\tilde{\eta}_k, p_s)$ for L84 hybrid levels in Fig. 2e at the indicated longitudes with progressively higher terrain. Thick gray curve marks $p_{k_p+1/2} \approx 86.7$ hPa ($k_p = 58$).

to avoid SAL-like thickness discontinuities across the $k_p + 1/2$ interface.

The L84 NOGHYB levels are plotted in Fig. 2e. Figure 6 plots the L84 shape factors $s(\tilde{\eta}_k, p_s)$ at various longitudes in Fig. 2e over progressively higher terrain. Note the roughly constant SAL-like shape factors at $0.4 \lesssim \tilde{\eta} \lesssim 1$ and the rapid transition to invariant shapes at $\tilde{\eta}_{k_p+1/2}$. Figure 7 plots the response of the L84 layer thicknesses Δp_k . While this coordinate produces a secondary thickness minimum over very high terrain (Fig. 7d), the profiles remain smooth and, in comparison to the corresponding plots for the SAL coordinate in Fig. 4, maintain smoothness and continuity of the thickness profiles at all model levels k .

4. New hybrid coordinates

The NOGHYB coordinate developed for NOGAPS-ALPHA was chosen to have the following:

- 1) a lowermost SAL model layer ($r_\sigma = 1$);
- 2) σ -like properties ($dB/d\tilde{\eta}$ constant) over the ~ 1000 –400-hPa range ($0.4 \lesssim \tilde{\eta} \lesssim 1$).

Since the analytical form in (30) originally designed for NOGHYB proves general enough to reproduce all the coordinates in section 3 (see Table 1), we use it here to develop two new hybrid coordinates that remove NOGHYB restrictions (1) and (2) above.

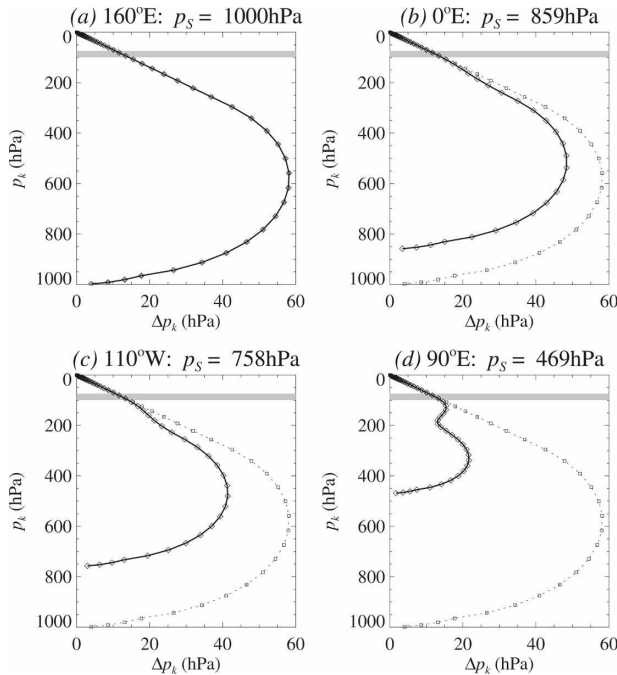


FIG. 7. NOGHYB coordinate response of layer pressure thicknesses Δp_k vs p_k (solid) relative to the L84 profile $\Delta \bar{p}_k$ at $p_S = p_0$ (dotted). Gray line makes $p_{k_p+1/2} \approx 86.7$ hPa ($k_p = 58$).

a. Relaxing the lower boundary limit: Coordinate NEWHYB1

Our first new coordinate (NEWHYB1) eliminates criterion (1) while retaining criterion (2). We achieve this by setting $r_p = 2.2$, $r_\sigma = 1.2$, $S = 5$, and $k_\sigma = 0$, the latter to avoid thickness discontinuities across the $L - k_\sigma + 1/2$ interface. The dashed curve in Fig. 8 plots $dB/d\tilde{\eta}$ for this coordinate. It reveals that the limiting surface index of $r_{L+1/2} = r_\sigma = 1.2$ yields a surface layer that is now neither a σ nor a SAL surface, so that criterion (1) no longer holds. However, $dB/d\tilde{\eta}$ remains roughly constant from $0.4 \leq \tilde{\eta} \leq 1$, satisfying criterion (2). The $r_p = 2.2$ limit provides a slightly smoother transition to isobaric layers than the original $r_p = 2$, since now $d^2B/d\tilde{\eta}^2 \rightarrow 0$ as $\tilde{\eta} \rightarrow \tilde{\eta}_{k_p+1/2}$ from below. Recall from (21) that vanishing $d^2B/d\tilde{\eta}^2$ implies local shape preservation of the thickness profiles.

Shape factors $s(\tilde{\eta}_k, p_S)$ in Fig. 9 retain near-perfect shape preservation from ~ 1000 to 400 hPa via a quasi-constant $s(\tilde{\eta}_k, p_S)$ profile, followed by a smooth transition to isobaric layers thereafter. The corresponding pressure thickness responses Δp_k in Fig. 10 remain similar in shape to the original profile over high terrain. The shape preservation properties of this new coordinate are evidently superior to those of NOGHYB (cf. Fig. 7).

b. Preservation of thickness profile shapes at all model levels: Coordinate NEWHYB2

Here we also relax criterion (2) and adjust parameters to attain a hybrid coordinate with the best shape preservation properties not just over the ~ 1000 –400-hPa range, but on all the terrain-following model levels $\tilde{\eta}_{k_p+1/2} < \tilde{\eta} < 1$.

This NEWHYB2 coordinate is identical to NEWHYB1, except we now set $r_\sigma = 1.35$ (see Table 1). This coordinate's $dB/d\tilde{\eta}$ profile is plotted as the dot-dashed curve in Fig. 8. The resulting shape profiles $s(\tilde{\eta}_k, p_S)$ in Fig. 11 now increase gradually over the ~ 1000 –400-hPa range and thus do not rigidly preserve thickness profile shapes. However, when applied over the whole profile, the net effects of the new coordinate in preserving the smooth nature of the thickness profiles are superior. Over the Himalayas, for example, the NEWHYB2 coordinate yields a compressed thickness profile Δp_k in Fig. 12d that better preserves the original thickness profile shape than the NEWHYB1 response in Fig. 10d. We have tested the two new coordinates with a range of other reference thickness profiles like those shown in Fig. 1a, and have found in each case that, of the three NOGAPS-ALPHA hybrids in Table 1, the NEWHYB2 coordinate consistently exhibits the best overall shape preservation over high terrain.

Even better shape preservation is obtained by increasing r_σ still further: for example, $r_\sigma = 1.5$ yields excellent shape preservation properties. However, these larger index values in turn yield larger values of $(p_S)_{\min}$, thus making the hybrid coordinate more prone to violation of monotonicity over high terrain. Since NOGAPS-ALPHA is an NWP prototype typically run

TABLE 1. The different vertical coordinates as implemented for NOGAPS-ALPHA L84. For all these coordinates $k_\sigma = 0$. Blank entries for S indicate that its value is not relevant in setting the coordinate's behavior since $r_p = r_\sigma$.

Settings	Vertical coordinates						
	σ	SAL	LG	CMAM	NOGHYB	NEWHYB1	NEWHYB2
r_p	1	1	2	1.5	2	2.2	2.2
r_σ	1	1	2	1.5	1	1.2	1.35
S	—	—	—	—	10	5	5
k_p	0	58	0	0	58	58	58

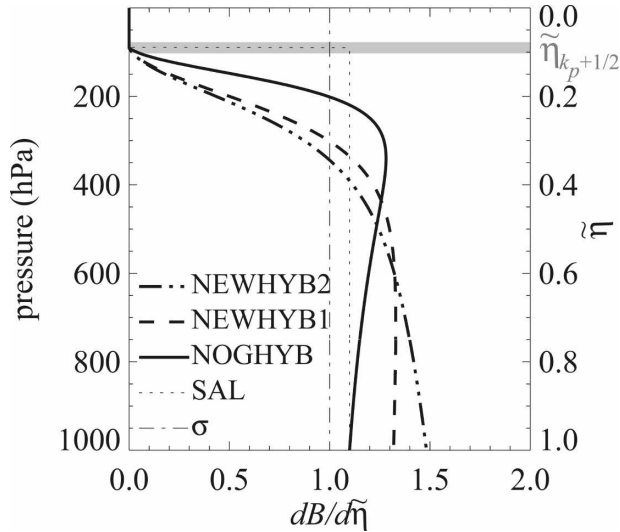


FIG. 8. Profiles of $dB/d\tilde{\eta}$ for the new hybrid coordinates discussed in section 4, with the NOGHYB, SAL, and σ values shown for reference (see Table 1).

at high horizontal resolution (see Eckermann et al. 2006), we settled on $r_\sigma = 1.35$ as a reasonable trade-off between shape preservation and robust monotonicity.

5. Errors in pressure gradient force over steep orography

In σ -coordinate models the pressure gradient force (PGF) is the sum of two terms. Over steeply sloping

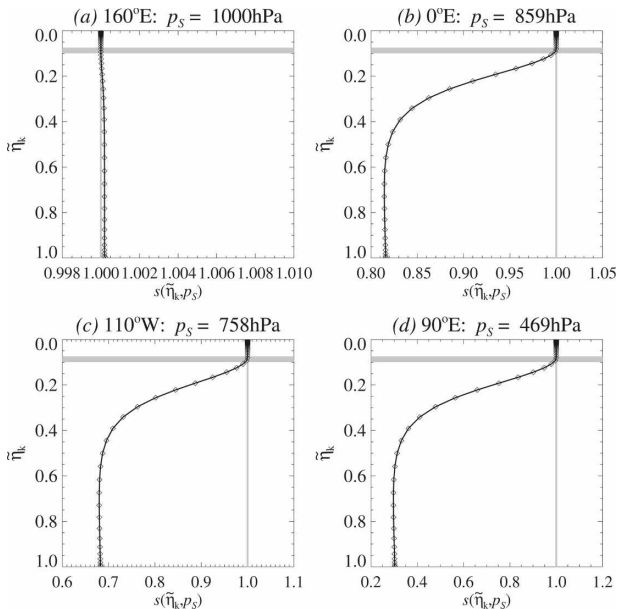


FIG. 9. NEWHYB1 coordinate shape factors $s(\tilde{\eta}_k, p_s)$ for L84 hybrid levels in Fig. 2f at the indicated longitudes with progressively higher terrain. Thick gray curve marks $p_{k_p+1/2} \approx 86.7$ hPa ($k_p = 58$).

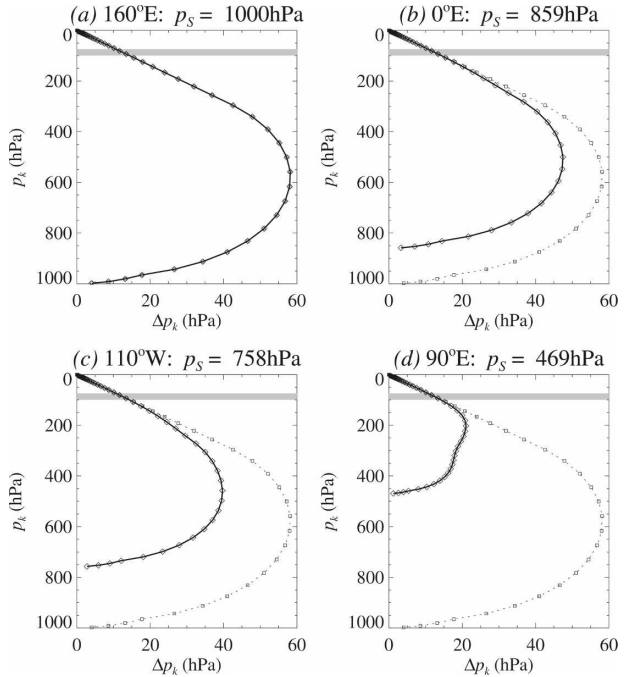


FIG. 10. NEWHYB1 coordinate response of layer pressure thicknesses Δp_k vs p_k (solid) relative to the L84 profile $\Delta \bar{p}_k$ at $p_s = p_0$ (dotted).

terrain, large hydrostatic corrections apply to both terms, making their values very nearly equal and opposite. The small PGF residual therefore becomes susceptible to the combined discretization and interpolation

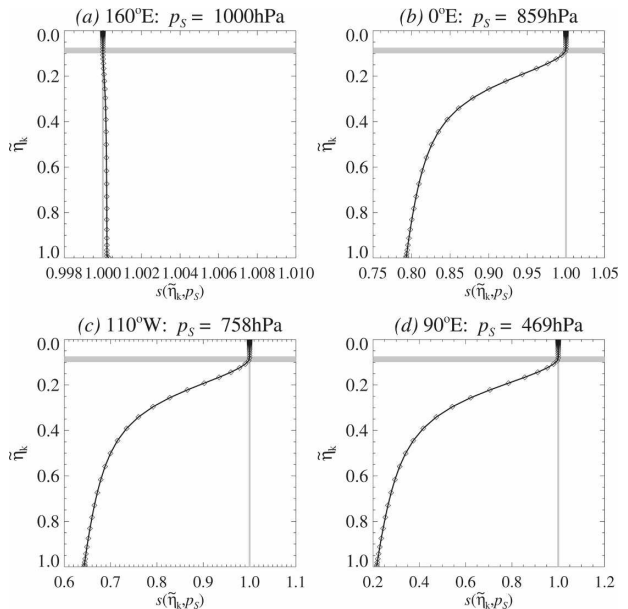


FIG. 11. NEWHYB2 coordinate shape factors $s(\tilde{\eta}_k, p_s)$ for L84 hybrid levels in Fig. 2g at the indicated longitudes with progressively higher terrain. Thick gray curve marks $p_{k_p+1/2} \approx 86.7$ hPa ($k_p = 58$).

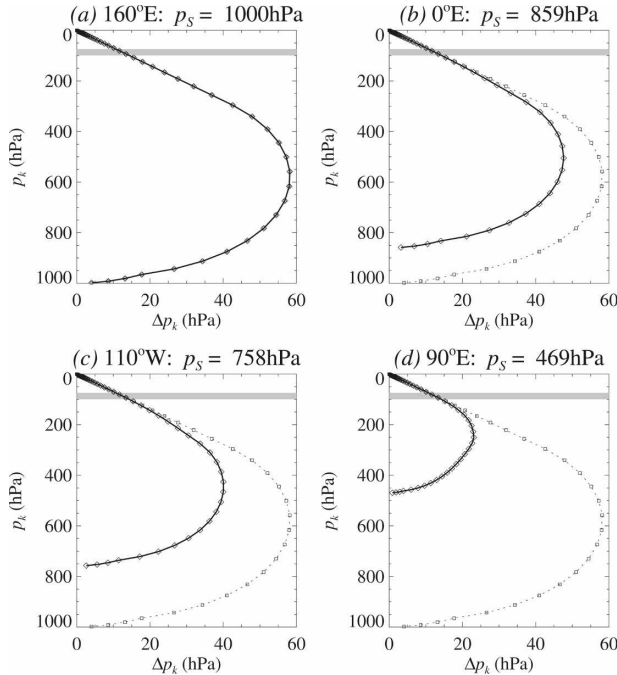


FIG. 12. NEWHYB2 coordinate response of layer pressure thicknesses Δp_k vs p_k (solid) relative to the L84 profile $\Delta \bar{p}_k$ at $p_S = p_0$ (dotted).

errors in each of these larger magnitude terms, as is well known (e.g., Corby et al. 1972; Gary 1973; Phillips 1974; Arakawa and Suarez 1983).

Simmons and Burridge (1981) found significant reductions in stratospheric PGF errors using hybrid coordinates. To facilitate comparisons with their results, here we evaluate their discretized error function $E_k(p_S)$ using their vertical temperature profile (Fig. 13a; see also Fig. 2 of Simmons and Strüfing 1981) and the same choice of a 10% surface pressure change over a 100-km horizontal distance. Figures 13b,c show resulting $E_k(p_S)$ profiles for the hybrid coordinates in Table 1 using our L84 model layers. As in Simmons and Burridge (1981), these values are plotted as geostrophic wind speed errors using a nominal Coriolis parameter $f = 10^{-4} \text{ s}^{-1}$. We show results for $p_S = 800 \text{ hPa}$. The abrupt increase in stratospheric temperatures leads to large stratospheric PGF errors using the σ coordinate. All the hybrid coordinates reduce these stratospheric errors while maintaining fairly small tropospheric errors. Figure 13c shows that the NEWHYB1 and NEWHYB2 coordinates yield the smallest stratospheric PGF errors of all the hybrid coordinates tested.

To investigate the generality of these findings, we allowed the analytical temperature profile to vary somewhat realistically. First we added normally distributed random offsets to the sea level and tropopause

temperatures of 3-K standard deviation, to stratopause temperatures of 5-K standard deviation, and random vertical offsets to the tropopause pressure height of 1-km standard deviation. Then, to each temperature profile j we superimposed a sinusoidal perturbation of the following form:

$$T'_j(Z) = T_{\text{peak}}(Z) \sin \left[\int_0^Z m_*(z) dz + \varphi_j \right], \quad (32)$$

$$T_{\text{peak}}(Z) = 1\text{K} \exp \left(\frac{Z - 10 \text{ km}}{2H_E} \right), \quad (33)$$

$$\lambda_*(Z) = \frac{2\pi}{m_*(Z)} = 2 \text{ km} \exp \left(\frac{Z - 10 \text{ km}}{2H_E} \right). \quad (34)$$

These equations mimic the vertical variation of the energy-containing gravity wave scales as defined by canonical vertical wavenumber spectra (see Figs. 2–3 of Smith et al. 1987), with parameters settings in (33) and (34) based on spectral analyses of long-term high-resolution radiosonde temperatures (e.g., Allen and Vincent 1995). We set $H_E = 2.3H \approx 16 \text{ km}$ following Fritts and Alexander (2003), and assign phases φ_j randomly between 0° and 360° . Ten perturbed temperature profiles resulting from this algorithm are plotted in Fig. 13d to convey the scale and range of the imposed variability.

The root-mean square errors (RMSEs) calculated from 500 such profiles using $p_S = 800 \text{ hPa}$ are plotted in Figs. 13e,f for the various hybrid coordinates. The overall trends seen in the top panels for the original temperature profile persist. In particular, the NEWHYB1 and NEWHYB2 coordinates yield the smallest stratospheric PGF errors.

6. Tests in a global model

In addition to PGF errors, hybrid coordinates can alleviate other sources of σ -coordinate errors that are not easily gauged by offline tests, such as errors in simulating vertical advection or sharp horizontal gradients (Konor and Arakawa 1997). Thus, here we implement a subset of the hybrid vertical coordinates introduced in sections 3 and 4 into a global spectral model and test their performance using direct model integrations. We use the forecast model component of NOGAPS-ALPHA, the high-altitude NOGAPS prototype, which is hydrostatic, Eulerian, spectral in the horizontal and finite difference in the vertical based on the L-grid discretization of Arakawa and Suarez (1983) (see also Hogan and Rosmond 1991). A vertical coordinate of Simmons and Strüfing's (1983) form in (6) is built into the dynamical core.

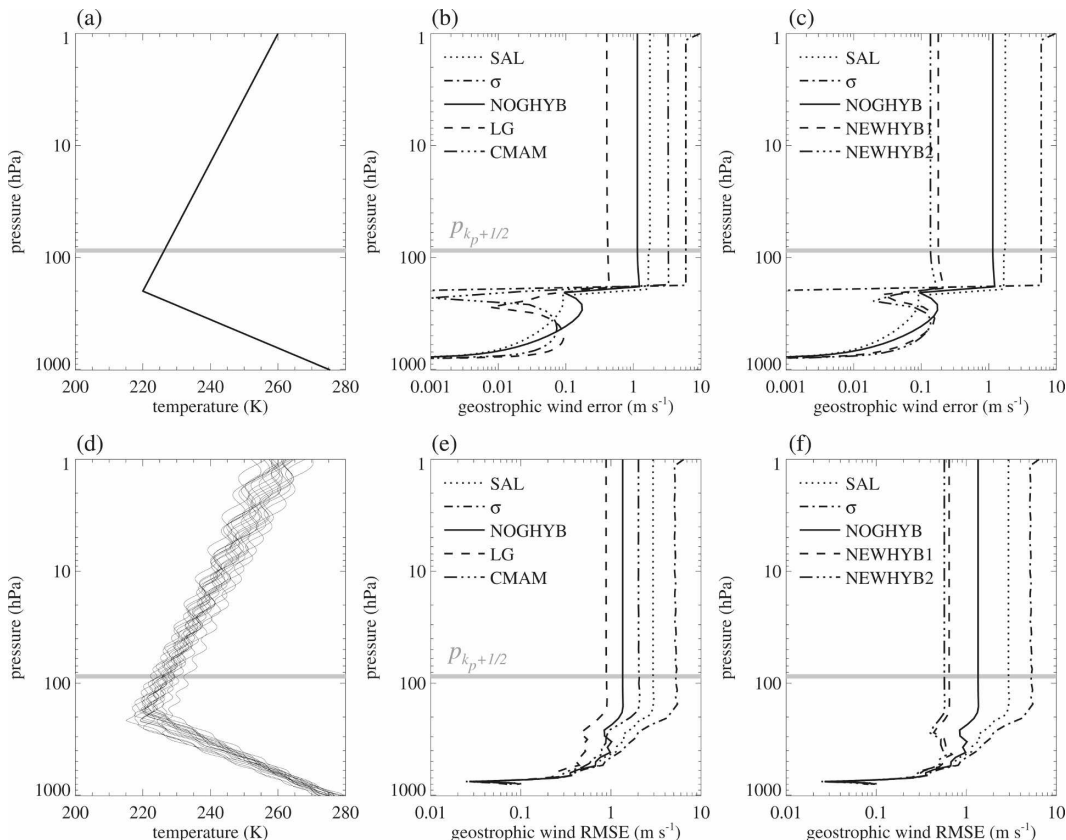


FIG. 13. For the idealized temperature profile in (a), (b)–(c) plot L84 geostrophic wind errors for the indicated coordinates based on the specific vertical discretization of Simmons and Burridge (1981): see their Eq. (6.1). (e), (f) Geostrophic wind RMSEs from 500 similar calculations applied to temperature profiles with stochastic variability added, as described in section 5; (d) 10 representative examples of the temperature profiles. All calculations used a surface pressure $p_S = 800$ hPa.

a. Idealized simulations

The adiabatic simulations using analytical initial conditions that are routinely used to test global models (e.g., Giraldo and Rosmond 2004) typically either omit terrain (Staniforth and White 2007) or prescribe specific planetary-scale terrain variations (Jablonowski and Williamson 2006). To test hybrid coordinates, we require states that support more realistic variable terrain. Static atmospheres in which temperature only varies vertically permit arbitrary terrain since, given an analytical temperature profile, hydrostatic integration yields corresponding analytical expressions for the required surface temperature and pressure as a function of terrain height needed to initialize this state. Static states also allow dynamical errors to be diagnosed directly from the simulated wind, divergence, and vorticity fields. T79L84 NOGAPS-ALPHA experiments using the linearly decreasing temperature profile in Giraldo and Rosmond (2004) maintained a

static state over 15 days using both ideal and realistic terrain. We then used the COESA (1976) temperature profile, which includes realistic middle-atmosphere variations as in Fig. 13a. We show results using the latter temperature initialization and realistic T79 orography only, as they are very similar to those using idealized terrain.

Figure 14 plots global RMSEs of relative vorticity and divergence versus forecast hour at 500, 100, and 10 hPa. These errors, while still small, are about two to three orders of magnitude larger than those using the linear temperature profile. The vorticity errors manifest over the terrain as vertically deep structures of short horizontal scale, consistent with the PGF errors discussed in section 5. Like the offline PGF estimates in Fig. 13, the vorticity errors are largest for the σ coordinate at all levels, and are one to two orders of magnitude smaller when using the NEWHYB1 or NEWHYB2 coordinate.

Divergence errors in Fig. 14 are also largest using σ

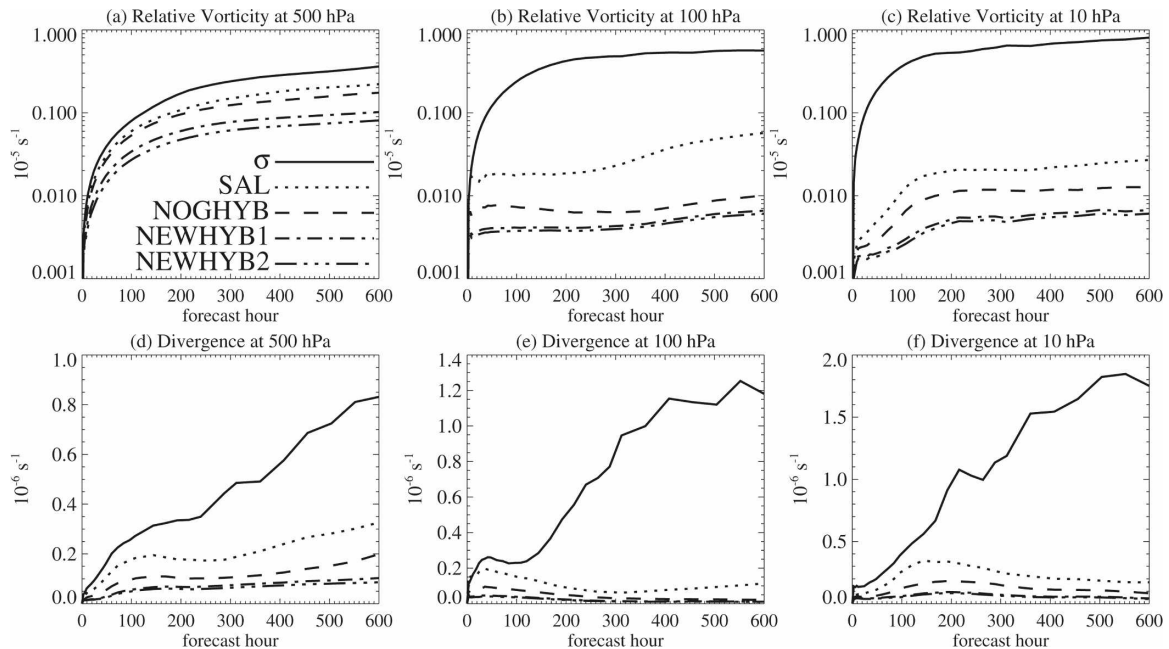


FIG. 14. Variation with forecast time of global RMSEs in (top) relative vorticity and (bottom) divergence at (from left to right) 500, 100, and 10 hPa for idealized T79L84 NOGAPS-ALPHA experiments using different vertical coordinates: σ (solid), SAL (dotted), NOGHYB (dashed), NEWHYB1 (dot-dashed), and NEWHYB2 (solid-dashed).

coordinates. They aggregate over high steep terrain such as the Andes and Himalayas as short shallow divergence structures, very similar to the spurious stratospheric divergence structures reported by Trenberth and Stepaniak (2002) over high-terrain in σ -based reanalysis fields. The results in Fig. 14 support the contention of Trenberth and Stepaniak (2002) that these anomalies should be substantially reduced by using hybrid coordinates. Again, the error suppression is greatest at all altitudes when using the NEWHYB1 or NEWHYB2 coordinate.

b. Stability of the semi-implicit time scheme

NOGAPS achieves longer model time steps by treating gravity wave propagation semi-implicitly. The algorithm, described in section 7.2 of Hogan et al. (1991), closely follows the discretized three-time-level (leap-frog) implementation of the Robert et al. (1972) method by Hoskins and Simmons (1975), as subsequently generalized to hybrid vertical coordinates by Simmons and Strüfing (1981). Following Hoskins and Simmons (1975), the algorithm linearizes around a reference temperature profile $T_r(\tilde{\eta})$. Based on the stability analysis of Simmons et al. (1978), NOGAPS uses an isothermal reference temperature profile of $T_r(\tilde{\eta}) = 300$ K (Hogan et al. 1991), the same choice used in the hybrid coordinate version of the ECMWF model (Simmons et al. 1989).

Extension of this scheme to hybrid coordinates involves linearization about a reference surface pressure, p_r , as well (Simmons and Burridge 1981). Since NOGAPS uses σ levels operationally, the choice for p_r has not been critical to the stability of the scheme to date (see, e.g., Table 3 of Simmons and Burridge 1981). Hogan et al. (1991) adopted $p_r = 600$ hPa, based on calculations suggesting a small stability advantage in using p_r values near the minimum anticipated terrain pressures in the model. In testing various types of hybrid coordinates, however, Simmons and Strüfing (1981) found that the stability of the semi-implicit scheme became sensitive to the value of p_r .

Simmons et al. (1978) and Simmons and Strüfing (1981) modeled the stability of their semi-implicit time scheme offline by using the idealized vertical temperature profile in Fig. 13a, thereby simplifying the problem to a matrix eigenvalue equation that they solved numerically (see appendix A of Simmons et al. 1989). Here we test the stability of the NOGAPS semi-implicit time scheme by running NOGAPS-ALPHA and monitoring its output. We favor this “brute force” approach over simpler offline eigenvalue computations since the latter provides only broad guidance, tends to overestimate the scheme’s stability relative to full model implementations (Simmons et al. 1978), and sometimes yields results counter to the experience from model runs (Simmons et al. 1989).

TABLE 2. Standard NOGAPS model time steps Δt (s) and their corresponding integer fractions of 1 h.

Δt (s)	1800	1200	900	720	600	450	400	360	300	240	200	180	150	120	100
1 h/ Δt	2	3	4	5	6	8	9	10	12	15	18	20	24	30	36

We test model stability by running the same T79L84 experiment in every case. The run is initialized with archived analysis fields at 0000 UTC 14 January 2003 and run out for 46 days to 0000 UTC 1 March. In common with other models, NOGAPS-ALPHA generally updates its radiative heating and cooling rates only every 1 or 2 h. In order that radiation and model time steps coincide, only model time steps Δt for which 1 h/ Δt is an integer are permitted. Table 2 lists the allowed values, and we run with those successively smaller time steps until a stable 46-day model integration is achieved. A stable run is identified if all model fields remain finite over the entire 46 days. The resulting stable Δt values are listed in Table 3 as a function of hybrid coordinate and p_r . To assess overall performance objectively, Table 3 also compiles scores by adding Δt values in each row and column.

Table 3 reveals instability for every coordinate when $p_r = 500$ hPa. Similar uniform instability at $p_r = 500$ hPa was noted in the eigenvalue solutions of Simmons and Strüfing (1981) and Simmons and Burridge (1981). At 600 hPa (the current default NOGAPS setting), the σ , SAL, CMAM, and NOGHYB coordinates yield stable integrations at $\Delta t \sim 600\text{--}720$ s, whereas the LG, NEWHYB1, and NEWHYB2 coordinates only yield stable integrations at much smaller time steps. Thus, the transition from σ to progressively more aggressive hybrid coordinates gradually reduces the low-end range of p_r values for which the semi-implicit time scheme is stable at acceptably long model time steps. This is reflected in the column scores along the bottom row of

Table 3, which are large for σ and small for NEWHYB2 and LG. Interestingly, the highest column score occurs for the NOGHYB coordinate. Since NOGHYB was designed as a first hybrid replacement for σ levels in NOGAPS-ALPHA (see section 3d), the results in Table 1 indicate that it offers no stability penalty (indeed, slight advantages) relative to σ at any $p_r \geq 600$ hPa. This objectively confirms anecdotal experience with this coordinate in NOGAPS-ALPHA, which, since it was implemented, has yielded stable integrations in a variety of short- and long-term simulations at the default NOGAPS setting of $p_r = 600$ hPa (Allen et al. 2006; McCormack et al. 2006; Eckermann et al. 2007a).

Furthermore, for $p_r \geq 700$ hPa the NEWHYB1 and NEWHYB2 coordinates also exhibit equal or superior stability to σ . The highest row scores in the far-right column of Table 3 occur for $p_r = 800$ hPa, indicating that this value yields the highest overall stability of the semi-implicit time scheme for all the hybrid coordinates tested. This is a robust result, evident in Table 3 for σ levels all the way through to the most aggressive hybrid coordinates like LG and NEWHYB2. These findings are consistent with the choice of $p_r = 800$ hPa in the corresponding ECMWF scheme (Simmons et al. 1989).

The outlier is the SAL coordinate, which is the only coordinate tested that does not exhibit a regular trend in stability as a function of p_r in Table 3. As discussed in section 3b, the large abrupt discontinuities in layer thicknesses at $p_{k_p+1/2}$ (see Figs. 4 and 5) lead to inaccurate vertical finite-difference calculations that reduce

TABLE 3. Longest model time steps Δt (s; see Table 2) yielding stable integration of the 46-day NOGAPS-ALPHA T79L84 hindcast, as a function of vertical coordinate (see Table 1) and p_r . Total “scores” are given in the bottom row and right column by adding Δt values along the indicated column and row, respectively. Table entry “U” denotes unstable integrations for all model time steps listed in Table 2 and is assigned a score of zero.

p_r	Vertical coordinates							Tot score
	σ	SAL	CMAM	NOGHYB	NEWHYB1	NEWHYB2	LG	
500 hPa	U	U	U	U	U	U	U	0
550 hPa	600	240	100	100	U	U	U	1040
600 hPa	600	720	600	720	200	150	100	3090
700 hPa	600	720	600	720	720	600	600	4560
800 hPa	720	600	600	720	720	720	720	4800
900 hPa	600	450	600	720	720	600	600	4290
1000 hPa	600	720	600	720	720	600	600	4560
1100 hPa	600	600	600	720	600	600	600	4320
Tot score	4320	4050	3700	4420	3680	3270	3220	

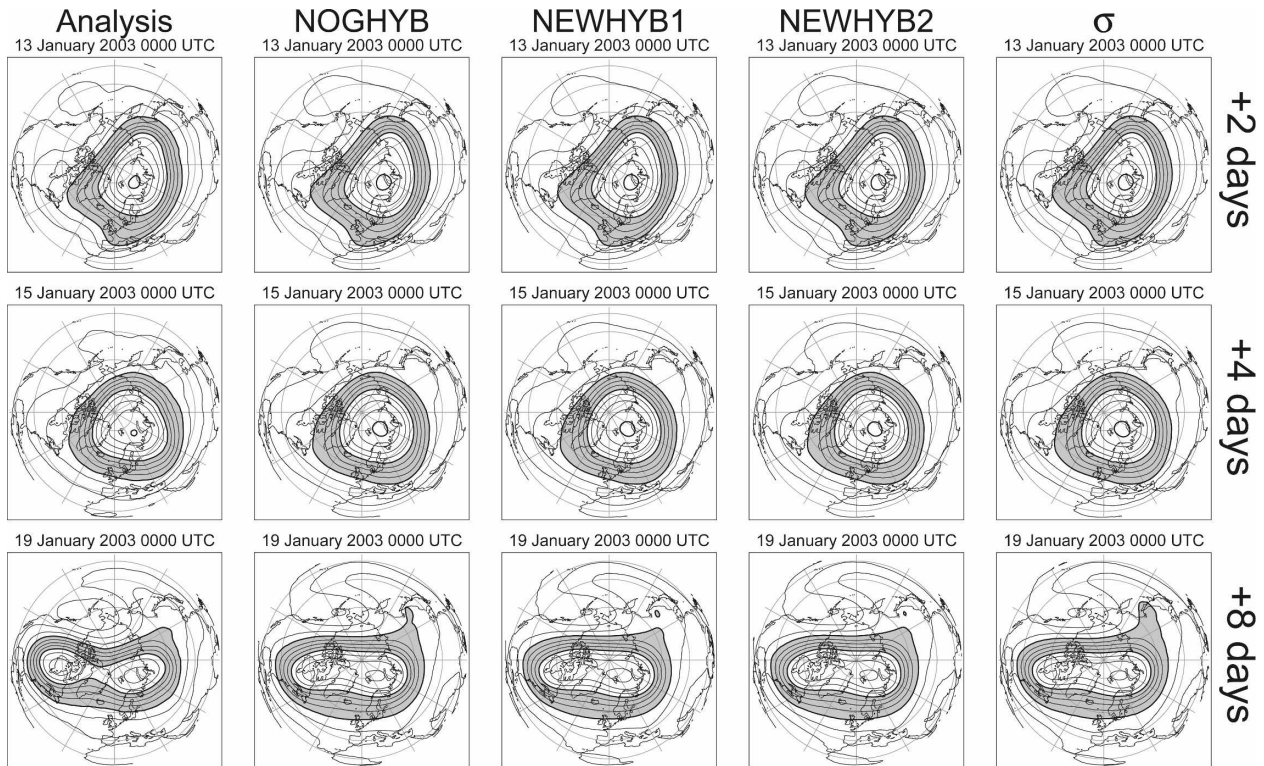


FIG. 15. Northern Hemisphere 50-hPa geopotential heights at 0000 UTC (top) 13, (middle) 15, and (bottom) 19 Jan 2003. (left) NOGAPS reanalysis fields. Remaining plots show NOGAPS-ALPHA T239L84 + 2-, +4-, and +8-day forecasts initialized with NOGAPS/GMAO reanalysis fields at 0000 UTC 11 Jan 2003 using NOGHYB, NEWHYB1, NEWHYB2, and σ vertical coordinates (columns 2–5, respectively). Contour interval is 160 m with the range 19 440–20 080 m shaded gray.

the stability of the semi-implicit time scheme (see section 7 of Simmons and Burridge 1981). Indeed, Simmons and Strüfing (1983) found that the ECMWF model was more prone to instability with the SAL coordinate than with any other coordinate they tested, consistent with the results in Table 3.

Thus, changing p_r from 600 to 800 hPa in NOGAPS-ALPHA provides optimal model stability over the broad range of hybrid coordinates tested in Table 3. More specifically, this change allows the NEWHYB1 and NEWHYB2 coordinates to be implemented and tested in NOGAPS-ALPHA without incurring any stability penalty relative to σ .

c. Forecast skill

To assess the overall impact of each hybrid coordinate in NOGAPS-ALPHA, we performed T239L84 forecasts using each coordinate, initialized at 0000 UTC for each day of the period 6–30 January 2003. We chose this period because of the range of stratospheric dynamics that occurred. The early parts of January 2003 contained strong stratospheric vortex winds (see Fig. 8 of Eckermann et al. 2007b), which present well-known

challenges for model stability (e.g., Simmons et al. 1989). In mid-January there was a major stratospheric warming (McCormack et al. 2004; Blum et al. 2006) of the split-vortex type (Charlton and Polvani 2007), like the February 1979 warming focused upon in the hybrid coordinate tests of the ECMWF model by Simmons and Strüfing (1983) and the February 1994 warming in the forecasting study of Lahoz (1999). Since warmings present the greatest stratospheric forecasting and stability challenges for NWP models (Vaugh et al. 1998; Lahoz 1999; Simmons et al. 2005), this period provides a stringent test of model stability and forecast skill.

As both initial states and verifying analysis for the forecasts, we use NOGAPS reanalyses (1000–10 hPa) from the T239L30 operational (σ coordinate) system using the Naval Research Laboratory (NRL) Atmospheric Variational Data Assimilation System (NAVDAS), the National Aeronautics and Space Administration's (NASA's) Global Modeling and Assimilation Office (GMAO) analyses (10–0.4 hPa), and a relaxation to climatology above the 0.4-hPa level. Details on the blending and model initialization of these fields are given in section 3.1.2 of Eckermann et al. (2006).

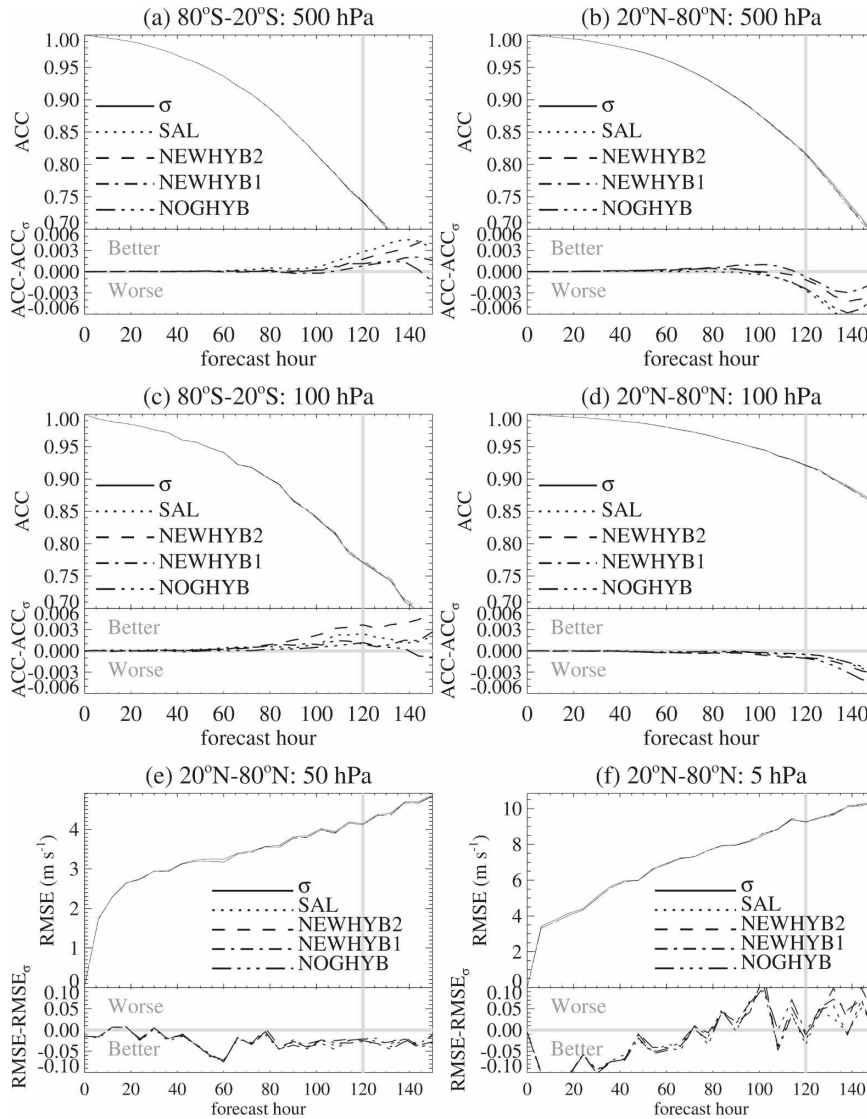


FIG. 16. (top two rows) Mean geopotential height ACCs and (bottom row) horizontal wind RMSEs vs forecast hour (6-h resolution) for T239L84 NOGAPS-ALPHA forecasts from 6 to 30 Jan 2003. (top insets) Results for different vertical coordinates: σ (solid), SAL (dotted), NOGHYB (solid-dashed), NEWHYB1 (dot-dashed), and NEWHYB2 (dashed). (bottom insets) Differences between the latter four curves and the σ curve, with signs that signify better or worse skill than the σ forecast highlighted in each case in gray. Results are shown for (a) 500 hPa 20°–80°S, (b) 500 hPa 20°–80°N, (c) 100 hPa 20°–80°S, (d) 100 hPa 20°–80°N, (e) 50 hPa 20°–80°N, and (f) 5 hPa 20°–80°N.

Each forecast ran out 10 days, with output saved every 6 h. The forecasts all used $p_r = 800$ hPa based on the results in Table 3. As an example, Fig. 15 shows 50-hPa geopotential heights from +2-, +4-, and +8-day forecasts initialized on 11 January using different vertical coordinates, with the NOGAPS/GMAO reanalysis fields shown in the left column. The +8-day forecasts capture the onset of a split-vortex warming. To assess the skill of all the forecasts over this 25-day period objectively, we computed mean errors (bias), mean ab-

solute errors, RMSEs, and anomaly correlation coefficients (ACCs) using standard area-weighted formulas (see section 2 of Waugh et al. 1998).

Figure 16 plots time-mean geopotential height ACCs for these forecasts at 500 (top row) and 100 hPa (middle row) in the 20°–80° latitude band in each hemisphere. The geopotential height climatology used in these calculations was the 15-yr January mean of the NCEP Department of Energy (DoE) Second Atmospheric Model Intercomparison Project (AMIP II) reanalysis

(Kanamitsu et al. 2002). There is very little difference among the ACCs of the various coordinate forecasts, even beyond 5 days. Similarly small (neutral) model impacts of hybrid coordinate forecasts relative to σ forecasts were noted by Simmons and Strüfing (1983). The small differences are expanded in the bottom panel of each plot by plotting the difference in each hybrid coordinate's ACC from the ACC of the σ -coordinate forecasts. These plots reveal small positive impacts in the Southern Hemisphere and small negative impacts in the Northern Hemisphere. Although all these trends are very weak, close inspection shows that the NEWHYB1 and NEWHYB2 coordinate forecasts have small systematic positive impacts relative to the other hybrid coordinate forecasts.

Figures 16e,f show stratospheric horizontal wind RMSEs in the 20°–80°N band. Since the error analysis in sections 5 and 6a indicates that differences should be largest over high variable terrain, these RMSE calculations used winds only from those model grid points where the underlying terrain was >1000 m. While RMSE differences are again very small, overall the hybrid coordinate RMSEs are systematically lower than the σ reference. This appears to be consistent with the idealized PGF error estimates in Figs. 13 and 14.

7. Summary and discussion

Perhaps the central result of this study is clarification of the role of $dB/d\tilde{\eta}$ in defining salient characteristics of hybrid coordinates of the Simmons and Strüfing (1983) form in (6). In diagnosing coordinate properties using $dB/d\tilde{\eta}$ -based tests of monotonicity and preservation of the smoothness and shape of layer thickness profiles, it became clear that there are no obvious optimal choices for this profile: each choice has specific advantages and disadvantages.

For example, robust shape preservation and monotonicity competitive with σ levels suggests a SAL or NOGHYB coordinate with constant or near-constant tropospheric $dB/d\tilde{\eta}$ values. Yet this property then requires a very sharp transition in the lower stratosphere to yield isobaric model layers in the middle atmosphere (Fig. 3), which distorts layer thickness profiles over high terrain in the upper troposphere and lower stratosphere (see Figs. 4, 5, and 7). This, then, would seem to argue for hybrid coordinates incorporating a smoother variation in $dB/d\tilde{\eta}$ with height, such as the LG coordinate. Yet for these coordinates, the integral constraint on $dB/d\tilde{\eta}$ from the boundary conditions (10),

$$\int_{\tilde{\eta}_{k_p+1/2}}^1 \frac{dB}{d\tilde{\eta}}(\eta') d\eta' = B(1) = 1, \quad (35)$$

implies necessarily larger maximum $dB/d\tilde{\eta}$ values that render these coordinates nonmonotonic at larger $(p_s)_{\min}$ values. The final choice involves a trade-off between these and other competing concerns, and thus will vary from model to model. For instance, low-resolution climate models need worry less about the monotonicity criterion implied by maximum $dB/d\tilde{\eta}$ values than high-resolution NWP systems.

In choosing a coordinate it is instructive to review the choices made in other models. Some analytical choices were reviewed in section 3. More commonly, however, modeling studies simply tabulate their discretized $A_{k+1/2}$ and $B_{k+1/2}$ values. Direct inspection of these values is not particularly illuminating and, thus, is of limited guidance to other modelers. However, $dB/d\tilde{\eta}$ can readily be evaluated from such tabulations, which, we have argued, provides all the salient information about the nature of the hybrid coordinate. With this understanding, we can compute and plot $dB/d\tilde{\eta}$ values for different models.

Figure 17 plots $dB/d\tilde{\eta}$ profiles computed from quoted $B_{k+1/2}$ coefficients used in some well-known global climate models, with the source of these values cited in each example in the figure caption. Unsurprisingly, based on our previous discussion, hybrid coordinate choices vary widely among the models. For example, Fig. 17a immediately reveals that the Community Atmosphere Model (CAM) and Whole Atmosphere Community Climate Model (WACCM) use a SAL coordinate (cf. Fig. 3). Additionally, we see that their lowest model layer is set to pure σ ($dB/d\tilde{\eta} = 1$), which produces a small low-level thickness discontinuity, in addition to the standard SAL thickness discontinuity at $p_{k_p+1/2}$.

Similar $B_{k+1/2}$ tabulations for NWP systems are harder to find in the scientific literature. Figure 18 plots $dB/d\tilde{\eta}$ profiles from six different versions of the ECMWF IFS, obtained from $B_{k+1/2}$ tabulations made publicly available on the ECMWF Web site, and those from the GMAO Goddard Earth Observing System (GEOS4) and the German Weather Service model obtained from technical reports. The ECMWF results reveal a history of periodically swapping between two different types of hybrid coordinate, while always asymptoting to a pure σ layer at the surface. The German NWP formulation mirrors one of these two ECMWF choices (as does the ECHAM5 formulation in Fig. 17e). The pure σ layer at the surface of the GEOS4 model produces a sharp discontinuity in layer thicknesses between the two lowest layers in this model.

We developed and analyzed two new hybrid coordinates (NEWHYB1 and NEWHYB2) as potential replacements for the current NOGHYB coordinate in

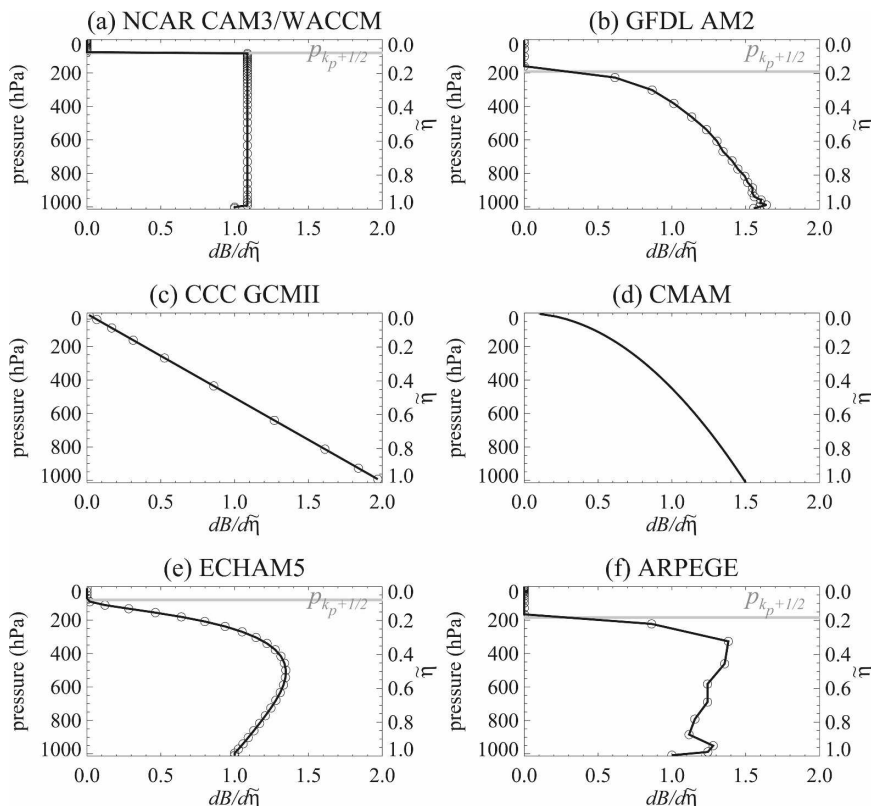


FIG. 17. Profiles of $dB/d\tilde{\eta}$ used in selected climate models: (a) CAM3/WACCM (Collins et al. 2004); (b) GFDL AM2 (Table 2 of Anderson et al. 2004); (c) CCC GCMII (Table 1 of McFarlane et al. 1992); (d) CMAM [Eq. (1) of Polavarapu et al. 2005]; (e) ECHAM5 (Table 2.2 of Roeckner et al. 2003); and (f) ARPEGE (Table 1 of Déqué et al. 1994).

NOGAPS-ALPHA. Offline tests suggested these new coordinates offered significant improvements relative to NOGHYB in terms of shape preservation of layer thickness profiles (cf. Figs. 7, 10, and 12) and reduction of stratospheric PGF errors (Figs. 13c,f). While idealized NOGAPS-ALPHA experiments confirmed these error reductions (Fig. 14), detailed forecasting experiments indicated essentially neutral (weak positive) impact relative to NOGHYB and even σ forecasts. Slight destabilization of the semi-implicit time scheme was rectified by changing p_r from 600 to 800 hPa, yielding stability equal to or better than σ . Skill scores in terms of geopotential height ACCs and wind RMSEs all showed marginal differences, with small reductions in wind errors in the stratosphere. Similar neutral or weakly positive findings were reported by Simmons and Strüfing (1983), suggesting that model forecast errors are being dominated by other aspects of the system, such as initial conditions and physical parameterizations.

Thus, despite offline and idealized online evidence to the contrary, there is limited practical evidence emerg-

ing from short-term forecast integrations to forcefully recommend one hybrid coordinate choice over another. These findings in some sense objectively ratify the wide range of hybrid coordinates that has emerged naturally among the current generation of NWP and climate models (Figs. 17 and 18). The one clear exception to this statement is the SAL coordinate, which has rendered both NOGAPS-ALPHA and the ECMWF model of Simmons and Strüfing (1983) more numerically unstable than any other vertical coordinate, and thus seems to be worth avoiding. The following qualifying remarks also pertain. There has been no systematic investigation of the impacts of hybrid coordinate choice on either extended-range forecasts or climate integrations. Furthermore, the short-term forecasting tests of this study and of Simmons and Strüfing (1983) applied only to the forecast model component: both studies used archived analysis fields produced by a σ -coordinate model for forecast initialization and verification. The inclusion of hybrid coordinates within the full forecast-assimilation system is expected to yield further improvements in skill during the data assimila-

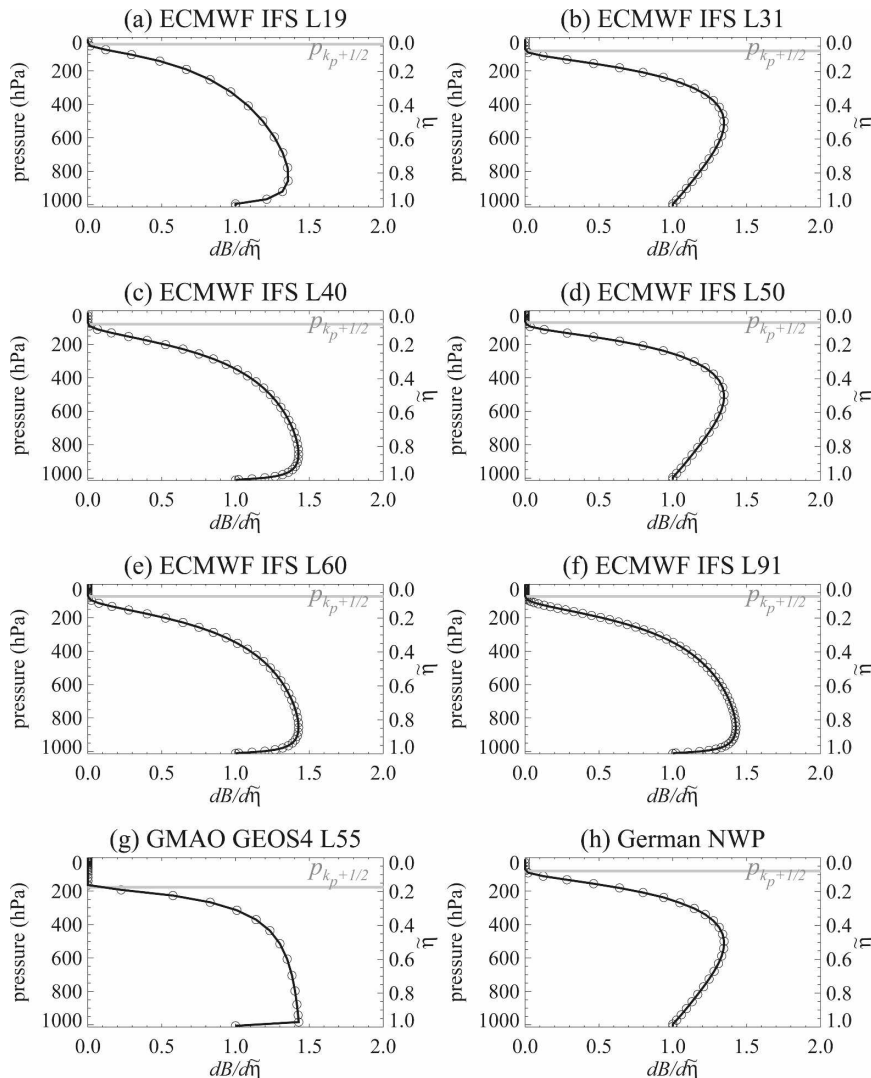


FIG. 18. Profiles of $dB/d\tilde{\eta}$ used in selected NWP models. Values from various generations of the ECMWF IFS that used (a) L19, (b) L31, (c) L40, (d) L50, (e) L60, and (f) L91 layer thicknesses (as tabulated online at <http://www.ecmwf.int>). Results for (g) GMAO GEOS4 L55 (Bloom et al. 2005) and (h) German Weather Service L31 Global-Modell (GME) (DWD 2004).

tion phase as well as improving the overall computational efficiency of the system (Simmons and Strüfing 1983; Trenberth and Stepaniak 2002). Given the large anomalies in stratospheric σ -coordinate analyses reported by Trenberth and Stepaniak (2002), hybrid coordinate effects on data assimilation appear to be worth studying in future investigations.

Based on the consensus of the tests reported here, we have recently changed the default hybrid coordinate in NOGAPS-ALPHA from NOGHYB to NEWHYB2, and changed the default p_r from 600 to 800 hPa.

Acknowledgments. This research was supported by the Office of Naval Research and the Defense Threat Reduction Agency. NCEP-DoE reanalysis 2 data were provided by the NOAA/OAR/ESRL PSD, Boulder, CO (see online at <http://www.cdc.noaa.gov>). Forecast runs were made possible by computer time at the Air Force Research Laboratory Major Shared Resource Center provided by the DoD High Performance Computing Modernization Program. I thank Tim Hogan for generating the NOGAPS reanalysis fields and Frank Giraldo for providing his test case subroutines.

APPENDIX

Algorithm for Assigning $A_{k+1/2}$ and $B_{k+1/2}$

The starting point is the model's predefined array of layer thicknesses $\Delta\tilde{p}_k$ (see Fig. 1a). Starting at the top half-level $p_{1/2} = p_{\text{top}}$, these thicknesses are integrated to generate interface pressures:

$$\tilde{p}_{k+1/2} = p_{\text{top}} + \sum_{i=1}^k \Delta\tilde{p}_i. \quad (\text{A1})$$

The thicknesses are normalized so that the reference

surface pressure $p_s = \tilde{p}_{L+1/2}$ in (A1) is ~ 1000 hPa. The corresponding half-level η values are then

$$\tilde{\eta}_{k+1/2} = \frac{\tilde{p}_{k+1/2} - p_{\text{top}}}{\tilde{p}_{L+1/2} - p_{\text{top}}}. \quad (\text{A2})$$

The algorithm requires specification of the number of isobaric layers at the top of the model, k_p , and number of purely σ -like levels at the bottom of the model, k_σ .

If $k_p \neq 0$, the k_p isobaric layers are set by assigning the interface coefficients as

$$\left. \begin{aligned} A_{k+1/2} &= \tilde{p}_{k+1/2} = p_{\text{top}} + \left(\frac{\tilde{\eta}_{k+1/2}}{\tilde{\eta}_{k_p+1/2}} \right) (\tilde{p}_{k_p+1/2} - p_{\text{top}}) \\ B_{k+1/2} &= 0 \end{aligned} \right\} k = 1, \dots, k_p. \quad (\text{A3})$$

Hybrid σ - p layers are set by the following relations that transition from a pure pressure interface at $k_p + 1/2$ to a pure σ -like interface at $k = L - k_\sigma + 1/2$:

$$\left. \begin{aligned} A_{k+1/2} &= p_{\text{top}} + (\tilde{\eta}_{k+1/2} - B_{k+1/2})(\tilde{p}_{L+1/2} - p_{\text{top}}) \\ B_{k+1/2} &= (b_{k+1/2})^{r_{k+1/2}} \end{aligned} \right\} k = k_p + 1, \dots, L - k_\sigma, \quad (\text{A4})$$

where $b_{k+1/2} = b(\tilde{\eta}_{k+1/2})$ is defined as the function:

$$b(\tilde{\eta}) = \frac{\tilde{\eta} - \tilde{\eta}_{k_p+1/2}}{1 - \tilde{\eta}_{k_p+1/2}}, \quad (\text{A5})$$

and the exponent r in the $B_{k+1/2}$ definition in (A3) is a function of $\tilde{\eta}$: $r_{k+1/2} = r(\tilde{\eta}_{k+1/2})$.

Finally, since some models include boundary layer

parameterizations that may be tuned specifically to σ levels, the algorithm allows the lowest k_σ model layers to be σ -like. However, use of the pure σ coordinate [(4)] for these levels would yield a discontinuity in layer thickness at the $L - k_\sigma + 1/2$ interface. If $r_{L-k_\sigma+1/2} = 1$, that discontinuity is removed by setting these k_σ lowermost levels as follows:

$$\left. \begin{aligned} A_{k+1/2} &= p_{\text{top}} + (\tilde{\eta}_{k+1/2} - B_{k+1/2})(\tilde{p}_{L+1/2} - p_{\text{top}}) \\ B_{k+1/2} &= \left(\frac{\tilde{\eta}_{k+1/2} - \tilde{\eta}_{k_p+1/2}}{1 - \tilde{\eta}_{k_p+1/2}} \right) \end{aligned} \right\} k = L + 1 - k_\sigma, \dots, L. \quad (\text{A6})$$

These surfaces are essentially equivalent to a σ -coordinate that levels out at a constant top pressure of $\tilde{p}_{k_p+1/2}$ instead of p_{top} : more formally, they are pure Sangster-Arakawa-Lamb (SAL) levels (see section 3b).

REFERENCES

Allen, D. R., S. D. Eckermann, J. P. McCormack, L. Coy, G. L. Manney, T. F. Hogan, and Y.-J. Kim, 2006: NOGAPS-ALPHA simulations of the 2002 Southern Hemisphere stratospheric major warming. *Mon. Wea. Rev.*, **134**, 498–518.

Allen, S. J., and R. A. Vincent, 1995: Gravity wave activity in the lower atmosphere: Seasonal and latitudinal variations. *J. Geophys. Res.*, **100**, 1327–1350.

Anderson, J. L., and Coauthors, 2004: The new GFDL global atmosphere and land model AM2-LM2: Evaluation with prescribed SST simulations. *J. Climate*, **17**, 4641–4673.

Arakawa, A., and V. R. Lamb, 1977: Computational design of the basic dynamical processes of the UCLA general circulation model. *Methods in Computational Physics: Advances in Research and Applications*, J. Chang, Ed., Academic Press, 173–265.

—, and M. J. Suarez, 1983: Vertical differencing of the primitive equations in sigma coordinates. *Mon. Wea. Rev.*, **111**, 34–45.

—, and C. S. Konor, 1996: Vertical differencing of the primitive equations based on the Charney-Phillips grid in hybrid σ - p vertical coordinates. *Mon. Wea. Rev.*, **124**, 511–528.

Bloom, S., and Coauthors, 2005: Documentation and validation of the Goddard Earth Observing System (GEOS) data assimilation system. *J. Geophys. Res.*, **110**, D08101, doi:10.1029/2004JD005426.

- lation system—version 4. NASA Tech. Memo. NASA/TM-2005-104606, 165 pp.
- Blum, U., G. Baumgarten, A. Schöch, S. Kirkwood, B. Naujokat, and K. H. Fricke, 2006: The atmospheric background situation in northern Scandinavia during January/February 2003 in the context of the MaCWAVE campaign. *Ann. Geophys.*, **24**, 1189–1197.
- Cariolle, D., and M. Déqué, 1986: Southern hemisphere medium-scale waves and total ozone disturbances in a spectral general circulation model. *J. Geophys. Res.*, **91**, 10 825–10 846.
- Charlton, A. J., and L. M. Polvani, 2007: A new look at stratospheric sudden warmings. Part I: Climatology and modeling benchmarks. *J. Climate*, **20**, 449–469.
- COESA, 1976: *U.S. Standard Atmosphere, 1976*. U.S. Government Printing Office, 227 pp.
- Collins, W. D., and Coauthors, 2004: Description of the NCAR Community Atmosphere Model (CAM 3.0). NCAR Tech. Note NCAR/TN-464+STR, 214 pp. [Available online at <http://www.cesm.ucar.edu/models/atm-cam/>.]
- Corby, G. A., A. Gilchrist, and R. L. Newson, 1972: A general circulation model of the atmosphere suitable for long period integrations. *Quart. J. Roy. Meteor. Soc.*, **98**, 809–832.
- Déqué, M., C. Dreveton, A. Braun, and D. Cariolle, 1994: The ARPEGE/IFS atmosphere model: A contribution to the French community climate modelling. *Climate Dyn.*, **10**, 249–266.
- DWD, 2004: Quarterly report of the German NWP-system. Part 2: Description of the German NWP system. Tech. Rep., Deutscher Wetterdienst, 31 pp.
- Eckermann, S. D., J. P. McCormack, L. Coy, D. Allen, T. F. Hogan, Y. J. Kim, and D. E. Siskind, 2004: NOGAPS-ALPHA: A prototype high-altitude version of the Navy's global numerical weather prediction model. Preprints, *Symp. on the 50th Anniversary of Operational Numerical Weather Prediction*; College Park, MD; NCEP and Cosponsors; P2.6. [Available online at <http://uap-www.nv.navy.mil/dynamics/papers/EckermannP2.6-reprint.pdf>.]
- , and Coauthors, 2006: Imaging gravity waves in lower stratospheric AMSU-A radiances. Part 2: Validation case study. *Atmos. Chem. Phys.*, **6**, 3343–3362.
- , D. Broutman, M. T. Stollberg, J. Ma, J. P. McCormack, and T. F. Hogan, 2007a: Atmospheric effects of the total solar eclipse of 4 December 2002 simulated with a high-altitude global model. *J. Geophys. Res.*, **112**, D14105, doi:10.1029/2006JD007880.
- , J. Ma, D. L. Wu, and D. Broutman, 2007b: A three-dimensional mountain wave imaged in satellite radiance throughout the stratosphere: Evidence of the effects of directional wind shear. *Quart. J. Roy. Meteor. Soc.*, **133**, 1959–1975.
- Eluszkiewicz, J., R. S. Hemler, J. D. Mahlman, L. Bruhwiler, and L. L. Takacs, 2000: Sensitivity of age-of-air calculations to the choice of advection scheme. *J. Atmos. Sci.*, **57**, 3185–3201.
- Fels, S. B., J. D. Mahlman, M. D. Schwarzkopf, and R. W. Sinclair, 1980: Stratospheric sensitivity to perturbations in ozone and carbon dioxide: Radiative and dynamical response. *J. Atmos. Sci.*, **37**, 2265–2297.
- Fritts, D. C., and M. J. Alexander, 2003: Gravity wave dynamics and effects in the middle atmosphere. *Rev. Geophys.*, **41**, 1003, doi:10.1029/2001RG000106.
- Gary, J. M., 1973: Estimate of truncation error in transformed coordinate, primitive equation atmospheric models. *J. Atmos. Sci.*, **30**, 223–233.
- Giraldo, F. X., and T. E. Rosmond, 2004: A scalable spectral element Eulerian atmospheric model (SEE-AM) for NWP: Dynamical core tests. *Mon. Wea. Rev.*, **132**, 133–153.
- Haltiner, G. J., and R. J. Williams, 1980: *Numerical Prediction and Dynamic Meteorology*. 2nd ed. Wiley & Sons, 477 pp.
- Hogan, T. F., and T. E. Rosmond, 1991: The description of the Navy Operational Global Atmospheric Prediction System's spectral forecast model. *Mon. Wea. Rev.*, **119**, 1786–1815.
- , —, and R. Gelaro, 1991: The NOGAPS forecast model: A technical description. Naval Oceanographic and Atmospheric Research Laboratory Rep. 13, 219 pp.
- Hoskins, B. J., and A. J. Simmons, 1975: A multi-layer spectral model and the semi-implicit method. *Quart. J. Roy. Meteor. Soc.*, **101**, 637–655.
- Jablonski, C., and D. L. Williamson, 2006: A baroclinic instability test case for atmospheric model dynamical cores. *Quart. J. Roy. Meteor. Soc.*, **132**, 2943–2975.
- Kanamitsu, M., W. Ebisuzaki, J. Woollen, S.-K. Yang, J. J. Hnilo, M. Fiorino, and G. L. Potter, 2002: NCEP–DOE AMIP II reanalysis (R-2). *Bull. Amer. Meteor. Soc.*, **83**, 1631–1643.
- Kasahara, A., 1974: Various vertical coordinate systems used for numerical weather prediction. *Mon. Wea. Rev.*, **102**, 509–522; Corrigendum, **103**, 664.
- Konor, C. S., and A. Arakawa, 1997: Design of an atmospheric model based on a generalized vertical coordinate. *Mon. Wea. Rev.*, **125**, 1649–1673.
- Lahoz, W. A., 1999: Predictive skill of the UKMO Unified Model in the lower stratosphere. *Quart. J. Roy. Meteor. Soc.*, **125**, 2205–2238.
- Laprise, R., 1992: The Euler equations of motion with hydrostatic pressure as an independent variable. *Mon. Wea. Rev.*, **120**, 197–207.
- , and C. Girard, 1990: A spectral general circulation model using a piecewise-constant finite-element representation on a hybrid vertical coordinate system. *J. Climate*, **3**, 32–52.
- McCormack, J. P., and Coauthors, 2004: NOGAPS-ALPHA model simulations of stratospheric ozone during the SOLVE2 campaign. *Atmos. Chem. Phys.*, **4**, 2401–2423.
- , S. D. Eckermann, D. E. Siskind, and T. J. McGee, 2006: CHEM2D-OPP: A new linearized gas-phase ozone photochemistry parameterization for high-altitude NWP and climate models. *Atmos. Chem. Phys.*, **6**, 4943–4972.
- McFarlane, N. A., G. J. Boer, J.-P. Blanchet, and M. Lazare, 1992: The Canadian Climate Centre second-generation general circulation model and its equilibrium climate. *J. Climate*, **5**, 1013–1044.
- Mintz, Y., 1965: Very long-term global integration of the primitive equations of atmospheric motion: An experiment in climate simulation. *Causes of Climatic Change, Meteor. Monogr.*, No. 30, Amer. Meteor. Soc., 20–36.
- Phillips, N. A., 1957: A coordinate system having some special advantages for numerical forecasting. *J. Meteor.*, **14**, 184–185.
- , 1974: Application of Arakawa's energy-conserving layer model to operational numerical weather prediction. National Meteorological Center Office Note 104, 40 pp. [Available online at <http://www.emc.ncep.noaa.gov/officenotes/>.]
- Polavarapu, S., S. Ren, Y. Rochon, D. Sankey, N. Ek, J. Koshyk, and D. Tarasick, 2005: Data assimilation with the Canadian middle atmosphere model. *Atmos.–Ocean*, **43**, 77–100.
- Robert, A. J., H. Henderson, and C. Turnbull, 1972: An implicit time integration scheme for baroclinic models of the atmosphere. *Mon. Wea. Rev.*, **100**, 329–335.
- Roeckner, E., and Coauthors, 2003: The atmospheric general cir-

- ulation model ECHAM5. Part I. Model description. Rep. 349, Max Planck Institute for Meteorology, 127 pp.
- Sangster, W. E., 1960: A method of representing the horizontal pressure force without reduction of station pressures to sea level. *J. Meteor.*, **17**, 166–176.
- Schlesinger, M. E., and Y. Mintz, 1979: Numerical simulations of ozone production, transport, and distribution with a global atmospheric general circulation model. *J. Atmos. Sci.*, **36**, 1325–1361.
- Simmons, A. J., and D. M. Burridge, 1981: An energy and angular momentum conserving vertical finite-difference scheme and hybrid vertical coordinates. *Mon. Wea. Rev.*, **109**, 758–766.
- , and R. Strüfing, 1981: An energy and angular-momentum conserving finite-difference scheme, hybrid coordinates and medium-range weather prediction. ECMWF Tech. Rep. 28, 68 pp.
- , and R. Strüfing, 1983: Numerical forecasts of stratospheric warming events using a model with a hybrid vertical coordinate. *Quart. J. Roy. Meteor. Soc.*, **109**, 81–111.
- , B. J. Hoskins, and D. M. Burridge, 1978: Stability of the semi-implicit method of time integration. *Mon. Wea. Rev.*, **106**, 405–412.
- , D. M. Burridge, M. Jarraud, C. Girard, and W. Wergen, 1989: The ECMWF medium-range prediction models: Development of the numerical formulations and the impact of increased resolution. *Meteor. Atmos. Phys.*, **40**, 28–60.
- , M. Hortal, G. Kelly, A. McNally, A. Untch, and S. Uppala, 2005: ECMWF analyses and forecasts of stratospheric winter polar vortex breakup: September 2002 in the Southern Hemisphere and related events. *J. Atmos. Sci.*, **62**, 668–689.
- Smith, S. A., D. C. Fritts, and T. E. VanZandt, 1987: Evidence for a saturated spectrum of atmospheric gravity waves. *J. Atmos. Sci.*, **44**, 1404–1410.
- Staniforth, A., and A. A. White, 2007: Some exact solutions of geophysical fluid-dynamics equations for testing models in spherical and plane geometry. *Quart. J. Roy. Meteor. Soc.*, **133**, 1605–1614.
- Trenberth, K. E., and D. P. Stepaniak, 2002: A pathological problem with NCEP reanalyses in the stratosphere. *J. Climate*, **15**, 690–695.
- Waugh, D. W., J. M. Sisson, and D. J. Karoly, 1998: Predictive skill of an NWP system in the southern lower stratosphere. *Quart. J. Roy. Meteor. Soc.*, **124**, 2181–2200.
- Webster, S., J. Thuburn, B. Hoskins, and M. Rodwell, 1999: Further development of a hybrid-isentropic GCM. *Quart. J. Roy. Meteor. Soc.*, **125**, 2305–2331.
- Wood, N., and A. Staniforth, 2003: The deep-atmosphere Euler equations with a mass-based vertical coordinate. *Quart. J. Roy. Meteor. Soc.*, **129**, 1289–1300.
- Zhu, Z., J. Thuburn, B. J. Hoskins, and P. H. Haynes, 1992: A vertical finite-difference scheme based on a hybrid σ - θ - p coordinate. *Mon. Wea. Rev.*, **120**, 851–862.